LAPP-EXP 95-07
CPPM 95-02
ISN 95-108
LPC 95-51
October 1995

The Bugey 3 neutrino detector

M.Abbes [d], B.Achkar [b], S.Ait-Boubker[b], R.Aleksan[e], M.Avenier[b], G.Bagieu[b], J.Ballansat[a], Ch.Barnoux [b], R.Bazzoli[c], J.Berger[a], M.Bermond[a], P.Besson[a], M.Billault[c], J.Boucher[d], J.Bouchez [e], M.Bouriant [b], R.Brissot [b], B.Camberlin[a], J.F.Cavaignac [b], Ph.Charvin[e], J.Collot [b], A.Commerçon[c] ,M-C.Cousinou [c], J.P.Cussonneau [d], G.Daguin-Moynot[a], Y.Declais [a], Th.Desanlis [e], J-M.Dubois[a], Y.Dufour [d], G.Farrache [c], J.Favier [a], Y.Gally[c], F.Garciaz [c], L.Giacobone[a], B.Guerre-Chaley[b], J-P.Jobez[d], D.Jourde[e], E.Kajfasz [c], H.de Kerret [d], D.H.Koang [b], B.Lefièvre [d], F.Léon[c], E.Lesquoy [e], J.Mallet [e], A.Menthe[b], A.Metref [a], J.Mullié[e], E.Nagy [c], M.Obolensky [d], P.Ollive[c], A.Oriboni[a], H.Pessard [a], F.Pierre [e], J.Poinsignon[e], R.Potheau[c], R.Provasi[b,†], A.Stutz [b], J.Thion[a], J-F.Thomas[e,†], J.P.Wuthrick [d,†]

[a] *Laboratoire d'Annecy-le-Vieux de Physique des Particules, LAPP, IN2P3-CNRS, BP 110, F-74941 Annecy-le-Vieux, CEDEX, France*
[b] *Institut des Sciences Nucléaires, IN2P3-CNRS, F-38026 Grenoble, CEDEX, France*
[c] *Centre de Physique des Particules de Marseille, Faculté des Sciences de Luminy, IN2P3-CNRS, F-91288 Marseille, CEDEX 09 France*
[d] *Collège de France, Laboratoire de Physique Corpusculaire, IN2P3-CNRS, F-75231 Paris, CEDEX 05, France*
[e] *CEA, DAPNIA, Service de Physique des Particules, CE Saclay, F-91191 Gif-sur-Yvette, CEDEX, France*

Abstract

The Bugey 3 experiment, designed to measure oscillations of reactor neutrinos, has used 3 identical detection modules, each of 600 liters, filled with a new ^{6}Li-loaded liquid scintillator. These modules were located in two shielding bunkers, respectively 15 and 40 meters away from the reactor core. We describe here the mechanical characteristics of these modules, their shielding, the associated electronics, the trigger, the acquisition systems, the calibration and monitoring of these detectors, and the Monte Carlo simulations of their response to particles. We conclude on the overall performance of this new detection technique which has allowed the recording of 120000 neutrino interactions with good neutron efficiency (49 %), low background (2.5 evts/ hour) and good energy resolution (4 % at 4.4 MeV).

(*Submitted to Nuclear Instruments and Methods*)

†*deceased*

1 Introduction

Since the discovery of the $\bar{\nu}_e$ by Reines and Cowan[1], nuclear reactor sites remain a very attractive place for low energy neutrino experiments. Their very intense flux of anti-neutrinos ($1.8 \cdot 10^{17} \bar{\nu}_e$ by thermal Megawatt) allows the use of relatively low size and low cost detectors at the 1 ton scale for high statistics experiments on difficult issues such as the search for neutrino oscillations.

Benefiting from the hospitality and financial help of the French Electricity Company (EDF), as well as the very convenient possibility to work 13.6 meters away from a 2800 MW reactor core, a first series of experiments on neutrino oscillation were performed between 1981 and 1987[2], [3]. This program has been extended to a new set of measurements using novel detectors at 15 and 40 meters from the core of reactor 5 of the Bugey plant. During two years of data taking (1991-1992), we recorded about 120000 anti-neutrino events with the set-up described here; their analysis, published in ref.[4], shows no oscillation and extends substancially the exclusion domain of reactor experiments. One interesting feature was the possibility to run at two distances simultaneously which allowed to minimize the influence of the reactor anti-neutrino spectrum uncertainties in the analysis.

In the following we describe the detector principles, the mechanical design, the shielding, the electronics (photo-multipliers, signals processing, trigger and acquisition), the calibrations and monitoring (neutrons, gammas, light pulser), the Monte-Carlo simulation (neutron capture and positron measurement), and we describe the performances in neutrino measurement.

2 The detector principles

Three different classes of neutrino detectors have been used in various experiments, which all take advantage of the following inverse neutron β- decay reaction

$$\bar{\nu}_e + p \longrightarrow e^+ + n \tag{1}$$

which has an energy threshold at 1.8 MeV. The positron energy ranges between 0 and 7 MeV, while the emitted neutron carries few tens of keV of kinetic energy. In a first approximation the positron energy is related to the neutrino energy by:

$$E_{\bar{\nu}} \simeq E_{e^+} + 1.8 MeV \tag{2}$$

The two 511 keV gammas from the positron annihilation can be detected and used, at least in principle, for the positron identification. The neutron will quickly thermalize, and be captured in a time interval depending on the effective thermal neutron capture cross-section of the medium.(10 to 200 μsec)

1. The "integral" detectors are pure neutron detectors and ignore the positron[5]. A typical design is a set of ^3He proportional tubes surrounded by a hydrogen rich medium (i.e water) which is the proton target. They can have an extremely low intrinsic alpha background and are insensitive to gamma rays, but do not benefit from the natural possible 2-fold coincidence of reaction (1) as well as use of the positron energy spectrum to reveal oscillations. They are used to measure the integral of the neutrino flux from a reactor. Their efficiency for the neutrino's neutron is about 0.50. They are not protected against neutron background, correlated or not with the reactor.

2. In the "heterogeneous, differential" detectors, the target protons are the hydrogen atoms of a liquid organic scintillator and the emitted light gives a signal proportional to the positron energy. Neutrons, after slowing down in the scintillator, are then detected in a separate set of ^3He filled proportional tubes or chambers [6]. These detectors benefit from the very good neutron signature of the ^3He detectors, but their efficiency is not better than 0.25, due to geometrical factors as well as neutron losses by capture on hydrogen. They can provide rejection against fast neutrons backgrounds by making use of pulse shape discrimination properties (PSD)[19, 9] of the liquid scintillator.

3. In the "homogeneous, differential" detectors the liquid scintillator is also used to detect neutrons by the addition of a neutrophage element[7]. Gadolinium loaded scintillator is a well known example of such a mixture. If one looses the advantage of ^3He gamma insensitivity, the efficiency can be larger than 0.5, the neutrophage thermal neutron capture cross-section being much larger than that on hydrogen. Furthermore, the time separating the neutron from the positron is as small as tens of μsec compared to hundreds of μsec for class 2 detectors, thus reducing the accidental associations. Gadolinium neutron capture gives a neutron signature of several gammas of about 8 MeV of total energy. This feature gives edge effect problems as well as a loose spatial neutron-positron correlation which make their use less convenient for small size detectors (1 ton scale).

At Bugey, the small room available for the shielding bunker in the nearby underground of the reactor limited the size of any detector, therefore imposed a solution with a minimum of edge effects. The Bugey 3 collaboration has investigated and finally adopted the choice of an "homogeneous" detector filled with a pseudocumene based liquid scintillator with an H/C ratio of 1.4, doped with 0.15% of ^6Li (in mass), for the two following reasons [8, 9, 10]:

- The thermal neutron capture reaction :

$$n_{therm} +^6 Li \longrightarrow \alpha +^3 H(Q = 4.8MeV) \tag{3}$$

  leads to a very good event spatial and time confinement, since the mean distance between the neutron capture and positron is $\simeq 6cm$, while the mean separation time is 30 μsec. These two features allow a decrease in the rate of accidentals due to the use of both time and space neutron-positron correlation, and offer a minimum of edge effects. Furthermore, the neutron efficiency for a fast neutron thermalized in the liquid can be as high as 72 %, including edge effects and unseen liquid volumes.

- The alpha and triton being strongly ionizing particles, therefore the strong quenching factor of the scintillator makes the 4.8 MeV of available kinetic energy to be detected effectively as a local energy deposition of a 0.530 MeV electron. The good pseudocumene PSD properties , associated with the capture energy line selection, provides a selective thermal neutron signature.

The main characteristics of this scintillator are listed in Table 1

Table 1: Ne320 liquid scintillator data

^6Li loading	0.15% in weight
Attenuation length at 440 nm	$260 \pm 30cm$
Light yield (% of anthracene)	31±5%
Number of detected photoelectrons	$\simeq 150/MeV$
density	0.926
refractive index	1.55
H/C	1.4
time constants	fast:$< 10nsec$;slow:$200nsec$

3 Description of one detector module

The general features of a detector module are the following: The 600 liters volume of liquid scintillator is optically divided in 8x8x85 cm^3 independent cells. Their lateral size is a compromise between the mean distance between the neutron capture and the positron, and the photo-cathode surface of available photo-multipliers. The length choice has been imposed by the existing shielding castle. Every cell is instrumented at each side by a photo-multiplier (Fig. 1). We have built 3 identical modules, one being installed at the 15 meters station, the other two being on top of each other at the 40 meters station. Because of the chemical reactivity of the NE320, the only materials we allowed to be in contact with the liquid are 316L stainless steel and Teflon. The amount of inactive material has been reduced to the minimum, in order to minimize the overall background due to gammas and fast neutrons produced by cosmic ray interactions around or in the shielding[3].

Tank and windows

The body of the tank is a 122×62×85 cm^3 box made of 4 mm thick stainless steel walls stiffened by welded square tubes. Two 18 mm thick flat flanges receive the windows and the photo-multipliers mechanical support(Fig.1). In order to minimize the possible chemical exchanges between the tank steel and the scintillator, the internal metal surface has been polished at the factory (granularity below 0.05 μm). Special care for cleaning has been taken at the end of machining (passivation and ultra-pure water rinsing)[11].

The two optical windows are each made of a 131×71 cm^2, $8mm$ thick acrylic glass plate. Their protection against the strong pseudocumene chemical attack is obtained by a $125\mu m$ FEP Teflon sheet [12], glued at room temperature with an optical glue[13]. Acrylic glass has been prefered to Pyrex glass for safety reason (no "sudden and complete" destruction), easiness of machining (bolt holes drilling), feasibility in our laboratory, very small natural radioactivity, despite a 12 % loss of light caused by the Teflon interface (absorption , and reflection due to its low refractive index 1.344 for large incident angles). The windows are glued on the flat free surfaces of the 7x14 PMs support matrix by adhesive tape. The optical contact of photo-multipliers is achieved using a silicone grease [14].

As shown in Fig.2, the liquid tightness is obtained by two symmetrical expanded Teflon joints on each side of the 68 bolt holes[15]. In this way, we minimized the flexion forces on the acrylic glass window which were a danger for a good and stable optical contact of the photo-multipliers close to the sides. A 20 g nitrogen pressure is maintained above the

liquid, two 50 g valves insuring the security. We encountered no leak problems for three years of operation.

Internal optical separation

The PSD technique demands the optimization of the amount of detected light without too much timing degradation, then imposes the use of total light reflection: this implies a small gap of gas to maintain it. The 98 light reflectors are immersed in the liquid; each of them is a 85×8.3×8.3 cm^3 tunnel manufactured in the following way:

A sandwich, as shown in Fig.3, is made of the superposition of the 5 following layers: two external 125 μm thick transparent FEP Teflon skins [12] with, inside, a 150 μm stainless steel foil which is the hard core, covered by 15 μm of high reflectivity aluminum. A polyamid veil ("Tulle", normally used for wedding dresses) is placed between Teflon and aluminum to avoid wet contacts which suppress total reflectivity. The two (larger) external Teflon foils are thermally sealed together, closing the layer of air needed for total reflection. For small light angles, the low refractive index of FEP Teflon is sufficient to establish the total reflection. The final shape of the tunnels is obtained by folding the sandwich on a specially adapted folding machine. These tunnels were tested in a pressurized water tank to eliminate possible leaks.

Teflon "FEP" has been chosen for its excellent chemical properties, good transparency in the scintillation light region[1] and very good aptitude for thermal sealing. More transparent products were tried, but had much worse heat sealing properties, making them inadequate to produce 400 tunnels without leaks. The production has been performed with a commercial thermal sealing machine modified to better stabilize the temperature and time sealing parameters.

The positioning of tunnels in the tank is obtained by two rigid stainless steel 2 cm deep grids located close to the windows, leaving a dead liquid thickness of 3.3mm between tunnels

4 The low-activity shielding

The Bugey nuclear power plant runs four Pressurized Water Reactors (PWR) of 2800 MW each. Two laboratories were installed close to reactor 5, for which the contribution to the neutrino flux of the other reactors is strongly reduced. The sensitivity of the ^6Li detectors has allowed us to extract the neutrino signal from reactor 4, located at 95 m away during a reactor 5 shut-down. One laboratory ('position 1', Pos1) is installed inside the basement of the reactor, 15 m away from the core. The second laboratory ('position 2', Pos2) is a concrete bunker built at the surface level, 40 m from the reactor 5 (see Fig.4). Reactor, cosmic radiation and radioactivity of the surrounding materials constitute three potential sources of detector background. In previous differential shielding measurements [3] we have shown that the neutrino-like events rate induced by reactor associated neutron or gamma flux is lower than 3 event $h^{-1}m^{-3}$ for an hypothetic detector of neutron efficiency 1. This value was measured inside the central cave just below the reactor core with a similar detector shielding. In the final experiment the closest position is protected by 6.2 m of concrete against the core radiations instead of 2.5 m for the central cave. Thus one can

[1]The nominal transparency for a 125 μ film is 0.96 ; this is an important parameter since the effective transparency is this number raised to the power of twice the mean number of light reflections which is about 4

confidently conclude that there is no reactor associated background. Obviously this is also true for the position 2 located outside the reactor building. Additional passive as well as active shieldings must reduce the two other background sources to the required levels.

4.1 Passive shielding

First of all the two laboratories have to be protected against the neutral and hadronic components of the cosmic flux. This is achieved in position 1 by the structures of the reactor building itself equivalent to 23 m of water while in position 2 (Fig.4), the concrete bunker has a 4 m thick roof (9.5 m.w.e) and 2.5 m thick walls (6 m.w.e). Then, against the surrounding natural radioactivity and cosmic- induced background, the following protection has been built: from outside to inside, 10 cm of lead are followed by 25 cm of water, a 5 mm B_4C layer and then by the veto counters.

The gamma flux reduction due to the lead wall added to the effect of the 25 cm water tanks was evaluated to be close to 100. However a factor 30 was measured with a 5" $\times$ 3" NaI crystal between 0.2 and 1.4 MeV, reaching rapidly 100 at 1.5 MeV . This reveals the effect of the radioactive impurities contained in the internal materials despite our effort to select rather low radioactive level materials. In particular about half of the $10^3\, counts\, s^{-1}$ of the neutrino detector singles rate above 200 keV is attributed to the ^{40}K contained in photo-tubes. In position 2, 15 cm of iron was preferred to 10 cm of lead as offering a comparable gamma attenuation factor, lower multiplicity factor in neutron production by muons [16] at a lower price.

The main purpose of the water tanks is to slow-down the fast neutrons originating from the cosmic ray interactions with the outer materials including the lead or iron shielding; then they are captured either by protons inside the water tanks or by boron atoms outside. Additionally the veto counters act like an extra 10 cm thick neutron moderator and absorber. During the Bugey 2 experiment [3], we measured, with the detector ^3He chambers, the attenuation factor of a similar shielding, to be 270 for the $Am - Be$ source fast neutron spectrum.

4.2 The veto counters

The neutrino detector is totally surrounded on 6 sides by veto counters at Pos2 while only 5 at Pos1. There the bottom side, taking into account the muon flux angular distribution and the rather large expected signal to background ratio, has been replaced by a polyethylene sheet of equivalent thickness to maintain the same efficiency to neutrino events. The liquid scintillator (NE235H[8]) is enclosed in a box made of 12 mm acrylic glass walls, whose typical size is 160x190x8 cm^3. In order to counterbalance the hydrostatic pressure, a few 4mm diameter stainless steel cross-pieces join the vertical walls, this solution strongly reducing the amount of inert material offered to interaction with cosmic rays close to the detector[17]. The whole counter is then inserted in a light-tight box made of honeycomb type material.

Light collection set-up was carefully designed in order to get a large discrimination factor between the muons and the other particles. The low muon counting rate allows to veto the long-lived secondary particles like neutrons (t=30 μs). On the contrary a large counting rate is measured with a low energy deposition corresponding mainly to gamma Compton interactions inside the 8 mm thick liquid scintillator.

In order to ensure a total covering of the neutrino detector only one photo-multiplier was used for each panel as can be seen in Fig.5. Fluorescent light guides of NE172 type[8] cover two of the four small sides of the parallelepiped box, the two others being covered by TiO_2 painted reflectors. In addition, although not essential for light collection, aluminised mylar foils are wrapped onto the large sides. The photo-multiplier used is the the green-extended photo-cathode version of the XP 3461 RTC. The excellent matching of the fluorescent guide light absorption spectrum with the NE235H emission and the photo-cathode response allowed a good light collection for these 2.5 m^2 counters which gave 14 measured photo-electrons/MeV for crossing muons. The strong signal variation (factor 3) with the photo-multiplier distance has been reduced to about 1.2 by the use of Monte-Carlo designed masks covering the wave-length shifters.

In Fig.6 is shown the high energy part of the spectrum obtained with the top counter. One can see three different regions. The upper part corresponds to the well separated muon signals. The lower part shows the effect of the hardware threshold on the tail of the gamma signals. Between the two the flat part cannot be precisely attributed. However coincidence experiments have shown that 20% of these events are associated with fast neutrons.

Rejection efficiencies

The muon efficiency was studied through the proportion of veto counter tagged events to muon events appearing in the neutrino detector. These latter events are defined as those hitting at least six different planes of the detector. In this evaluation a lower limit of 99.5 % is obtained. Veto counter pulses have been digitized, so the muon energy loss distribution, and position of the gamma/muon threshold have been surveyed each day. The vetos counting rates were found to be stable within less than 1% [18].

5 Some definitions and relations

On every cell, the measurement of the two charges Q_{right} and Q_{left} allows the deduction of the following information:

- The total charge:

$$Q_{tot} = C_e.Q_{right} + Q_{left} \tag{4}$$

  where C_e is a gain balancing coefficient obtained in calibration runs and defined as:

$$C_e = \frac{< Q_{left} >}{< Q_{right} >} \tag{5}$$

- The localization variable along the longitudinal z axis of a cell:

$$Z_q = \frac{C_e.Q_{right} - Q_{left}}{Q_{tot}} \tag{6}$$

  Z_q was found to be approximately linear with z and provides a z resolution ranging from 13 cm at 1 MeV to 9 cm at 4 MeV positron energy (F.W.H.M) for the best liquid.

- The compensated total charge
  For a fixed energy deposit, the measured total charge Q_{tot} varies with Z_q through an

approximate parabolic dependence with its minimum at the center of the cell. We had several tools to study and parameterize this dependence (see calibration section) so we can determine a polynomial function $F(Z_q)$ and use it to correct Q_{tot}:

$$Q_c = \frac{Q_{tot}}{F(Z_q)} \tag{7}$$

Q_c is the "*compensated charge*", independent of the position z, from which the deposited energy will be derived using the energy calibration coefficients.

- The Pulse Shape Discrimination

  Comparing the sum $Q_{right} + Q_{left}$ with its fraction Q_2 left after typically 25 $nsec$ will make us sensitive to the PSD property of the liquid.

  The ratio :

$$R_{psd} = \frac{Q_2}{Q_{right} + Q_{left}} \tag{8}$$

  is independent of z and was used for the thermal neutron characterization as well as for the electron identification.

6 Photo-multipliers, electronics, trigger and acquisition

As quoted in [4] and in the previous section, a neutrino-like event is defined by two successive light pulses given by a 'light', and a 'heavy' particle, both being well localized in space and time. Then we have to check for a delayed coincidence between two such particles. The particle identification is done using pulse shape criteria: the quantity R_{psd} will be higher for heavy than light particles. An anti-neutrino event then requires the occurrence of a neutron candidate: the R_{psd} value and the capture energy variable are in the correct window; no other cell should fire at the same time and no cosmic ray counter should give a signal within 0.5 μs. A positron candidate (a light pulse exceeding 200 keV energy) should then preceed the neutron candidate by at most 100 μs, and the two candidates should be in the same or adjacent cells (proximity criterion).

For each pulse above a given discrimination threshold occuring in any cell or cosmic veto detector, the whole detector is digitized. Each channel is digitized in a Flash-ADC and photo-multipliers charges are integrated by two different gates (one for total and one for the rear charges) [19, 9] leading to PSD information. The drawing of the electronics set-up is shown in Fig.7.

6.1 Photo-multipliers

The photo-multipliers (PMT) are XP3462 from Philips[20] with high quantum efficiency, low potassium activity, relatively low dark current and good rise time. Typical values are given in table 2. The first grid is polarized by a 15 Volt Zener diode to maintain good timing properties over a wide range of high voltage supply. To avoid power dissipation and consequent heating of the detector the resistance chain has a value of 3.8 MΩ which for a nominal 1600 V supply leads to a convenient current. The moderate gain is supplemented by a pre-amplifier (G=3.5) fixed on the socket. The magnetic field on every photo-multiplier site is less than 0.2 $Gauss$ due to a 1 mm thick mu-metal sheet added to the internal panels of the veto counters.

Table 2: XP3462's characteristics.

Nominal gain at 1350 V †	10^6	
Quantum efficiency †	27	%
Anode rise time †	2	ns
Window refractive index †	1.54	
Background noise above 0.3 PE	6.3±4.5	kHz
After-pulse rate (t<600ns)	0.6±0.3	%
^{40}K activity	9	Bq

†Data from ref.[20]

6.2 Discrimination and subsequent signals

As good timing stability is essential for an optimal PSD determination, all logical signals are derived from constant fraction discriminators (DFC) [21] with a typical threshold of 80 mV corresponding to 200 keV energy deposition. Each time a signal triggers a DFC, the time of occurrence and the pattern of hitted cells and veto counters are stored in 16-rank memories, with a time accuracy of 250 ns. Together with the integration gates (P1 and P2), the OR of the DFC outputs (S) and the OR of the veto counter discriminators (V), two signals are generated by home-made electronic cards for trigger purposes: 1) a unicity signal (U) whenever only 1 out of the 98 cells fired. 2) a proximity signal (P) whenever identical or adjacent cells have fired in two ranks separated in time by less than 100 microseconds (in practice, the current pattern is compared to the 3 previous ones, and the comparison is made separately on horizontal and vertical projections of the module, for speed and simplicity reasons; the wrong proximities which might occur in case of multiple hits are removed off-line).

6.3 Analog signal processing

The processing of analog signals is based on modules developed around hybrid gated integrators [22] (CTT C39 from ELMATEK [2]) associated with 15 MHz 8 bits flash ADC (model EF 8308 from Thomson) working in a single clock shot mode as a fast digitizer and 8 event depth memories. The whole process up to digitization and triggering decision, including current integration, takes about 2 μs. To reduce the number of channels each integrator is fed with the signal of 5 far-away elementary cells leading to 20 CAMAC modules. These 6 gated integrators give access to:

- Q_{left} and Q_{right}. (gate P1)
- Q_2 the late charge, used to obtain R_{psd}. (gate P2)
- $Q_1^\star$ and $Q_2^\star$, an amplification by a factor of 8 of $Q_{left} + Q_{right}$ and Q_2 to increase the sensitivity in the energy region of the neutron capture and to allow for a PSD selection at the trigger level.
- a Δt information derived by a internal TAC triggered by left and right pulses provides another way of longitudinal localization.

[2]ISN-Grenoble license

The chosen values are 500 ns for the total charge gate P1 , the late charge gate P2 being delayed by 25 ns and ending with P1.

The amplified $Q_1^\star$ and $Q_2^\star$ are used, after digitization by a 15 MHz FADC, to address a 64Kbit RAM used as a 256 bit $\times$ 256 bit matrix. These bits are Camac-loaded with 1 in the ($Q_1^\star$,$Q_2^\star$) region corresponding to the neutron capture; a "neutron" capture signal (N) is generated whenever a signal occurs in this region of interest.

6.4 100MHz Flash ADC

Each cell of the detector is associated with a channel of a 6 bits flash ADC device (TRW 1029 J7C) with a 100 MHz sampling rate working in triggered mode with 64 steps and a depth of 4 events. This module is described elsewhere [23]. The sensitivity of this system helped us in determining PSD in the low energy region, gave information on energy deposition below the DFC's threshold, and allowed the rejection of PMT after-pulses which can fake heavy particle by increasing the late charge.

6.5 Trigger

The triggering function is built using a programmable 256X8 bit RAM, programmable through CAMAC, using 8 input signals and 3 output signals. Most of the input signals have been already mentioned: the OR of the DFC outputs (S), the OR of the veto counters (V), unicity (U), proximity (P), neutron (N); capture (C) is described below; other input signals are related to our various calibration signals. The outputs are: acquisition trigger, either instantaneous or delayed (usually by 100 microsec), a special CAMAC trigger for some of the calibration system and an instantaneous auxiliary output (AUX).

As an example, our neutrino trigger requires U x P x N x S x $\bar{V}$ and delivers a delayed trigger so that we know what happened during the 100 microseconds following the neutron capture. A trigger for accidentals requires the coincidence C x P, where C is a 100 microsecond long "capture" signal generated (using the AUX output) by the input U x N x S x $\bar{V}$.

These two triggers were run in parallel during data acquisition. The table 3 gives, for one module, typical rates for the signals used in the trigger logic. The pattern of trigger inputs and outputs are stored in a 16-rank memory read at each trigger, allowing for checks on the proper functioning of this system.

Table 3: Individual typical rates (Hz)

"S" Single (>200 keV)	1000
"U" Unicity	700
"P" Proximity	20
"N" Neutron	200
"V" Vetos OR	180

6.6 Acquisition

At each experimental position the data acquisition is controlled by a Motorola MC 68030 based VME computer running VERSADOS. These are linked through Ethernet to a μVAX GPX II used as supervisor. This computer also receives data from the slow control, such

as temperatures, pressures, power supplies, counting rates, and thermal power of the reactors, through UTINET branches. The VME units are connected to electronics crates through a 5 MHz ECL daisy chained bus derived from the Fera Lecroy specifications. A temporary event memory accessed by this fast bus and the VME bus reduces the random aspect of data flow. In each crate the CAMAC bus is used for read-out, data are then collected by that fast bus. Before storing data on Exabyte cartridges, the following online filter was applied: rejection of cosmic showers giving high multiplicity events and finer neutron capture selection taking account of Z_q correction for the capture charge and of individual cell neutron calibration coefficients.

7 Calibrations and monitoring

Such a fully analogical detection system obviously requires a careful calibration procedure. The overall operations consist in:

- A daily measurement of all pedestals, stored in the on-line database
- A daily measurement of the overall opto-electronic gain of each photo-multiplier channel, by means of a light-pulser
- A monthly gamma source calibration of each cell to give the energy scale and PSD of the positron.
- A monthly neutron source calibration of each cell to define the neutron capture energy peak and PSD windows.

For the purpose of calibration operations, each module is surrounded in its middle plane by a small Camac controlled moving trolley mounted on a chain (see Fig.1). Therefore, the radioactive source can be automatically positioned at the desired locations, in sequential runs.

7.1 The light-pulser gain monitoring system

The entire system consists of a spark-gap light pulse generator, associated to a network of optical fibers, band filters, grey attenuators and light intensity monitoring detectors[24]. A schematic view of the network is shown in Fig.8

The light-pulser
We have chosen to design a nitrogen flushed spark-gap, due to the following requirements[25]:

- Short light pulses ($\leq 10\ ns$ rise-time, $22\ ns$ FWHM, total length $\leq 200ns$)
- Light spectrum permitting an adequate filtering to match the scintillator and the PM at their maximum of folded sensitivity
- High light output intensity (200 photo-electrons on each PM after filtering and about $6\ m$ of light fiber)
- Reliability (50000 pulses each day during two years)
- Low cost

The final design, shown in Fig.9, had its two electrodes made of 2 mm diameter tungsten rods; their active extremities were carefully ball shaped by partial fusion. The angle between the axis of the two electrodes is 90°; these two geometrical features permit a good stability of the emitted intensity and space location of the spark. The electrical gap is 0.6 mm, and the RC has been adjusted to get 50 pulses/second with a 6 KV dc voltage and a capacitance of $100pF$ made of RG316/U coaxial cable. A problem of igniting the discharge was efficiently solved by adding inside the spark-gap 50 becquerel of an alpha particle emitter. The nitrogen flushing was 10 liters/hour during sparking runs, while staying at 0.2 in standby. The pulse-to-pulse light fluctuation has a gaussian-like dispersion of 4%. The pulse shape fits in the positron PSD digitizers scale, and could be used to detect anomalies on this variable.

Optical network

After a band filtering ($450 - 500$ nm)[26] the light crosses a variable optical attenuator made of two Camac driven disks allowing a range from 0 to 90 db by step of 2 db. This device was used to measure the linearity of the opto-electronic chain. Before the attenuation mechanism, three optical fibers collect a very small fraction of the light scattered by a slightly diffusing glass plate crossed by the beam, and lead to a 150 AVP RTC photo-multiplier which monitors the spark-gap intensity during linearity runs. Then the light beam is made parallel by a lens and enters an optical "highway" made of 244 plastic optical fibers glued together at each extremity. This 3.8 m pipeline crosses the shielding bunker, separates itself in two branches to feed two optical fan-outs on each side of the detector. These multiplexers share uniformly the light between 196 fibers 'seeing' each detector photo-multiplier through the window, and to the 36 fibers leading to the six light monitoring devices.

Light-pulser monitoring

Each distribution box is housing one set of the following elements:

- One Hamamatsu S1723.04 photo-diode and its preamplifier; a $^{57}Co(122\ keV)$ X ray source stays in place for the photo-diode calibration.
- One 150 AVP RTC photo-multiplier calibrated by the cosmic muon energy loss in a rod of 100 cm^3 plastic scintillator.
- Another 150 AVP RTC photo-multiplier calibrated by a small NaI crystal associated with an ^{241}Am alpha source.

These informations allowed the normalization of each light pulse of the spark-gap with redundancy. Therefore, the intrinsic dispersion of the light source was reduced to less than 0.4 %. From the distribution of the renormalized light pulses of each detector channel, we can monitor accurately its opto-electronic gain (maximum position) as well as the transparency of the liquid (from the sigma of the distribution and its maximum position one deduces the number of photo-electrons).

7.2 Electron calibrations

Gamma source measurements

For each cell we measure the Compton peak of the 4.4 MeV gamma emitted by an *Am-Be* source which is also used in neutron calibration. We trigger on the total charge $Q_{left} + Q_{right}$ of the target cell with a 2 MeV threshold and we make use of the remaining part of the detector as an anti multi-Compton event protection, with a 200 keV threshold by cell. This enhances efficiently the backward Compton peak, as shown in Fig.10. The analysis is done on line: PSD is used to eliminate recoil protons coming from the *Am-Be* fast neutrons, the two PMT gains are equilibrated and the Z_q-compensated sum Q_c is plotted for a selection of the central region cell of 30 cm. We chose to define the peak position as the abscissa of the right side, 2/3 down from the maximum, this quantity being less sensitive to fit correlations between width and maximum. The corresponding deposited energy has been determined by Monte-Carlo implying the careful simulation of the cell and trigger condition (anti-multi-Compton) (see Monte-Carlo section). The result was 4.43 MeV$\pm$0.034(*syst*) for the peak position as defined above.

The bulk of information coming both from source calibrations and spark-gap daily runs are analyzed off-line. The first operation is the elimination of the light pulser fluctuation by the use of the light monitoring devices, themselves renormalized of their own gain variation by their daily calibrations. The variation of gain of each photo-multiplier is fitted by a polynomial between the dates of two main source calibrations, and final calibrations coefficients are interpolated with these polynomial shapes. The plots of Fig.11 show some examples of gain survey where the source measurements are also indicated.

The knowledge of the number of photo-electrons detected by each cell in spark-gap runs associated with the calibration coefficients allows the calculation of the effective number of photo-electron per MeV of our detector with a good precision ($\sigma = 1.5\%$). These numbers, averaged on the 98 cells of each module are shown in Table 4; they were very stable for module 2 and 3, but falling 4 % each month for module 1 affected by a bad chemical evolution of its liquid, responsible for a permanent decrease of the transmission length.

Table 4: Average effective number of photo-electrons/MeV

module 1 (start/end of data taking)	128 / 95
module 2	130 / 130
module 3	150 / 145

Errors on energy and PSD determination

The intrinsic energy resolution for a fully contained electron of 4.2 MeV is 4% for the best liquid, and 5% for the worst figure of module 1. In gamma calibrations, where edge effects affect these numbers, we obtained respectively 5.2% and 6.3%, which are the values of the sigmas of the right side of the calibration Compton peaks, well reproduced by Monte-Carlo.

For the positron measurement one has to include the dispersion on the energy deposited in the positron cell by the two annihilation gammas. We thus obtained for a neutrino

energy of 6 MeV an overall resolution of 4.8% (1 sigma) for module 3 and a corresponding number of 5.4% for module 1. Such numbers reasonably match the 'oscillation' L/E variable smoothing of 13.4% at 15 meters and 4% at 40 meters brought by the reactor and detector sizes.

We estimated our accuracy on the energy calibration control for one cell to a sigma of less than 1% (0.35% for about half of the channels). This last number reaches the statistical limits; the other channels, mainly on detector 2 and 3, were affected by some electronics fluctuations leading to a day-to-day bigger dispersion; these numbers are reduced by a factor 10 when averaging on the 98 cells of the module. Thus the main energy uncertainty comes from the Monte-Carlo determination of the position of the calibration peak, to which we attribute $\pm 0.8\%$ systematics, the same for the three detectors. This last error becomes negligible when comparing two positions energy spectra, while it contributes when comparing theoretical reactor neutrino spectra to the measured ones.

The electron PSD parameters are rather independent of the position along the cell, and their energy dependence follow photo-statistics. The electron PSD peak position decreases very slowly with energy, as we did verify on background out of time gammas in neutrino data, and we did not correct for it, only doing a global loss of efficiency correction. For recoil protons, the variation of the quenching effect of the scintillator leads to a variation of 24 percent between 0.3 and 4 MeV of the PSD peak position. If we define as usual the PSD separation power (merit factor) as:

$$F = \frac{D_{p-e}}{(fwhm_e + fwhm_p)} \tag{9}$$

where D_{p-e} is the distance between the PSD electron and proton peaks, and fwhm their respective full widths at half maximum, then we see on Table 5 that F is reasonably constant with the positron energy. The corresponding figures for the (neutron capture)-(electron) separation are 0.95 and 1.2 at the end of Mod1 and Mod3 operation[27].

Table 5: PSD factor of merit for different electron energies (module 1)

$E_{electron}$	F
0.8-1.6 MeV	0.94
1.6-2.5 MeV	1.14
2.5-3.5 MeV	1.16
3.5-4.2 MeV	1.07

Detector linearity

As already stated, the linearity control of each one of the opto-electronics channels was elaborated using the light-pulser and variable optical attenuator system, but we also measured it on several cells and modules with a set of different radioactive sources. To the first measurement, this adds the linearity of the scintillator itself (which may be not linear below 300 keV for several physical reasons: Cerenkov effect near threshold, quenching effect on end of range of electron, etc). For each source, we reproduced by Monte-Carlo the deposited amount of energy corresponding to the backward Compton peak and the anti-multi Compton trigger effect, as well as the light collection process. This simulation has to be the most complete possible: one can easily find here reasons for disagreements between

published data concerning the linearity of Ne213 liquid scintillator [28], since edge effects, environment effects, trigger simulation are most of the time energy -dependent. The data in Fig.12 show the results obtained in an average of four independent measurements (2 cells of detector 2 and 2 cells of detector 3). A good straight line fit is obtained, but with an apparent energy offset of 50 keV, which may be attributed to already mentioned physical reasons. The same results were obtained on 5 cells of detector 1.

7.3 Calibration of the response to thermal neutrons

A selective signature of the thermal neutron is essential in the background rejection and therefore requires refined calibrations of the detector response with an appropriate neutron source. In addition, this information was required to define the neutrino PSD matrices which were a major component of the trigger logic of the $\bar{\nu}_e$ acquisition.

Relatively pure thermal neutron events were obtained by tagging recoil protons originating from fast neutron interactions in our detectors, and by subsequently recording their captures that occured, on average, 30 μs later. The neutron live time in an energy range [0-10 MeV] is related to the ^6Li density of our scintillator and is to first order a constant throughout our detectors. The same $Am - Be$ source was used for this purpose and the neutron matrices were set in order to select signals corresponding to recoil protons. The acquisition trigger was vetoed by the occurrence of a pulse in the cosmic counters, and simultaneously required the identification of a recoil proton detected in a single cell. Pulses which produce the triggers as well as those arising within 100 μs following them, were read out and further analyzed by the acquisition computer. Because proximity both in space and in time is a crucial element to distinguish a thermal neutron once a recoil proton was identified, a moderate counting rate of single events was required to reduce accidentals. This was obtained by calibrating our detection modules by groups of four adjacent cells with the source located at approximately 30 cm away from the closest cell. On average, the counting rate of single events with a 200 keV threshold was typically $1 - 2\ kHz$. In addition, this also provided a longitudinal distribution of the neutron interaction vertices broad enough to study the evolution of the parameters of the neutron capture peak as a function of the longitudinal z-position in the cell. Preceeding the calibration of each group, the source was automatically moved around the detector to its relevant position using the source transportation system, and a measurement of the charge pedestals of the active cells was performed.

Given the low rate of the acquisition (10-50 Hz), an on-line event filtering for each separate group was performed. Thermal neutron candidates were chosen in a single cell. Events where the recoil proton and the thermal neutron that occured in two different cells situated along a diagonal were also rejected on the basis they were very unlikely with respect to neutron migration considerations. In order to throw out events obviously located far away from the region of interest, loose windows were applied on both the total and the delayed charges of the thermal neutron candidates.

At the end of each run, the characteristics of the thermal neutron PSD peak for each separate cell were extracted by a Gaussian fit as shown in Fig.13. In order to obtain the mean value of the position variable Z_q correctly centered on zero, the neutron source was placed in the median plane of the cells and the photo-tube gain equalizing coefficients C_e were computed cell by cell from the thermal neutron event sample. A 2.3 σ PSD cut was applied on the left side of the capture peak to eliminate the small residual gamma contamination of the sample. Fig.14 presents the relative neutron-proton position for this

selected thermal neutron sample, computed with the variable Z_q previously defined. The distribution has a Gaussian shape centered on zero and very small tails. The final neutron capture event set was selected by applying an additional $\pm 2.5\ \sigma$ cut on this relative position distribution. The total charge peak of the neutron capture finally obtained is represented, for a typical cell, in Fig.15. Also shown in Fig.16 is the variation of the central value of this peak as a function of the longitudinal position Z_q in the cell. A correction curve was determined by fitting a second order polynomial to the experimental points. Finally, normalization coefficients were computed cell by cell to obtain, after a correction for the longitudinal variation, the averages of the neutron capture peaks aligned to the same value. This peak summed over a complete detection module is presented in Fig.17.

The last step of the neutron calibration consisted in interpolating day by day the cell parameters measured monthly. The global relative evolution of a specific parameter was determined from the data accumulated over a detection module. This is illustrated in the case of the resolution of the total charge peak in the top part of Fig.18. Then, for each separate cell, the value of a calibration parameter at a given time was obtained by applying the relative evolution with the initial points taken at the values given by the calibrations:

$$a^j(t) = a_i^j G(t - t_i)$$

where $a^j(t)$ is the value of the considered parameter at the time t (in days) for the cell j, a_i^j is the latest measured value of this parameter for this cell j, $G(t - t_i)$ is a polynomial $(G(0) = 1)$ parameterizing the relative evolution of a,where t_i is the time (in days) of the latest calibration.

The quality of the overall neutron capture calibration procedure can be independently checked by verifying that the rate of the cosmic neutrons remained constant over the entire neutrino data taking period as it is shown in the bottom part of Fig.18.

8 Monte-Carlo simulations

To determine the acceptance of the detector to neutrinos events, we have to simulate:

- The slowing down of the neutron inside all materials of the detector and even outside the detector (veto region), until its thermalization and final capture. Also we have to reproduce the absolute neutron efficiency.
- The process of the positron slowing down with the best representation possible, as well as the interaction of the two annihilation gamma rays , and the gamma calibration procedure.
- Once we know the topology of all energy deposits in the active parts of the detector, the light collection and electronics response has to be simulated for each of them, in the neutrino capture cell and in those around. This will give access to trigger simulation, acceptance in positron energy and correction function $F(Z_q)$

The philosophy has been to generate MC events (with a statistic 10 times that one of the data), to apply to them the data analysis cuts and then to compare overall integrated number of events (absolute normalization) and the real and simulated positron energy spectra . The CERN GEANT program has been used for the detector geometry description with modifications needed by our low energy phenomena.

8.1 The neutron slowing-down and capture program

The program [29] is able to track individual neutrons in an energy range of 0.001 eV to 10 MeV , loosing its energy by elastic collisions in the different materials of the detector (scintillator, iron, acrylic glass etc). The chemical bounds of hydrogen are approximated according to a semi-phenomenological model [30]. At thermal energy, a Maxwell distribution is used to represent the target nuclei and neutron motions at the detector mean temperature. Scattering and capture cross sections are taken from the BNL compilation [31]. The interaction with the light guide walls has been simulated and found negligible; only a small mean correction on the neutron efficiency has been applied for neutron captured in the 0.015 mm of stainless-steel. The validity of our program is established by several checks:

- The capture time: The agreement is good; the mean time between positron and neutron capture is found to be $29.7 \pm 0.2 \mu sec$ on real neutrino data, while Monte-Carlo gives $30.2 \pm 0.2 \mu sec$.(Fig. 19)
- Neutron efficiency has been checked in measurements using the $Am-Be$ source where one recoil proton was tagged (see neutron calibration section), with or without the 4.4 MeV gamma in coincidence on a NaI detector. We found on five different cells a mean efficiency of $0.687 \pm 0.011(syst. + stat.)$, the Monte-Carlo prediction being 0.696 (for a time window of $100 \mu sec$).
- Fig. 20 shows the comparison between measured neutron efficiency by tagged neutrons and the Monte-Carlo prediction as a function of the fast neutron energy measured by time-of-flight; this test has been done on a prototype cell in the Laboratoire Souterrain de Modane, where gamma and neutron natural background were strongly reduced.

8.2 Positron slowing-down and gamma interaction simulation

These processes have been carefully worked out since the lateral size of one cell is relatively small compared to the ranges of few cm of the positron which can easily interact or cross the cell walls (at 2 MeV the positron range is 1.5 cm and 25 % of them reach the cell walls). Furthermore, the two photons of the positron annihilation at rest or in flight have to be tracked also since they can deposit their energy in the positron cell itself or in others. We used the GEANT CERN program [32]. It has been improved by one of us [33] for electron tracking below 1 MeV. Specifically, the backward scattering of electrons on metal sheets is now much better reproduced, as verified on two experiments on the transmission and backward scattering of electrons and positron of 159 to 960 keV in metallic foils [34, 35]. These modifications are standard now in GEANT version $\geq$ 3.12. All trackings (positrons and photons) have been done down to 10 keV (where photoelectric cross-section is dominant). We found a mean energy deposited by the positron annihilation inside its origin cell of 176 keV, with a variance of 180 keV entering in the positron energy resolution (see previous section on gamma calibration)[27].

8.3 Simulation of the light collection and electronics

A Monte-Carlo program has been developed to simulate the light propagation in the optical system compound of the scintillator, the light-guide (Teflon FEP, nitrogen, aluminum), the window(Teflon FEP, acrylic glass) and the photo-multiplier (optical grease

and Pyrex). The validity of this simulation is based on the reproduction of a series of measurements using collimated gamma sources, and a Compton backward scattering set up (NaI coincidence). The result is shown in Fig.21 showing the charge detected by one cell photo-multiplier for different source positions along the longitudinal cell axis. The MC reproduces the distribution with a residual accuracy better than 1.2 %. The inputs of the program are all the involved refractive indices, attenuation of the liquid as a function of wave length, spectra of photo-cathode sensitivity and scintillator emitted light, attenuation of the Teflon foils and reflective power of aluminum. Associated with the measured number of photo-electrons at the center of the cells (measured each day), and applying simulation of the digitization by electronics, we were able to generate the polynomial coefficients used to describe the correction function $F(Z_q)$. This has been checked on cosmic neutrons where such coefficients are found experimentally, and there were no neutron peak capture differences when correcting for Z_q effect by the experimental coefficients or by the Monte-Carlo ones. Results of this Monte-Carlo have been used for real data positron Z_q correction. For module 1 for which the liquid attenuation length had a time-dependence, a set of correction coefficients was calculated each month, following the simulation of the daily measured numbers of photo-electrons per MeV.

With the help of the multi-Compton simulation associated with the light collection and digitization simulation, we evaluated the energy deposit corresponding to our fitted parameter of the Compton calibration peak (abscissa of the 2/3 of the peak maximum, as defined in the gamma calibration section). Two independent multi-Compton generators have been used, and both agreed to the final result within 0.2%. Variations of critical Monte-Carlo parameters have permitted to fix our systematic error on the energy scale: cells geometry, dead zones, quenching in the electron energy loss, range-energy relations, $Am - Be$ fast neutrons interaction producing gammas in the shielding and in the detector, cell thresholds in the anti-multi-Compton trigger, liquid attenuation length, effective number of photo-electrons/MeV. The result was 34 keV($syst.$) at 4.3 MeV, as already mentioned.

9 Performance of the detector

The remaining neutrino-like background surviving to the passive and active shielding can be divided in two categories: accidental events whose contribution is permanently measured using our auxiliary trigger and time-correlated events which are measured during the reactor-off periods.

9.1 Off-Line Data Reduction

In order to minimize these background with a good efficiency for the neutrino signal a set of analysis cuts has been optimized.

Triggers are rejected if a cosmic ray counter gave a signal in the preceding $100\mu s$. This induces a dead-time of about 2% for the experiment. Using results of neutron calibrations, an elliptical cut at 2.2 sigmas in the Energy versus PSD plane is applied to neutron candidates. The positron cell is defined as the one where the highest energy is deposited in case several cells were fired adjacent to the neutron cell. The positron energy is required to be between 1 and 6 MeV with no simultaneous energy deposit bigger than 1.5 MeV outside the positron cell. A 3σ cut is performed on the PSD of the positron candidates. Proximity criteria between the positron and neutron candidates are then applied: the positron can-

didate should precede the neutron candidate by at most 60 μs, the two candidates should be either in the same cell or in adjacent cells having a common face, and their separation in z should be smaller than 35 cm.

9.2 Accidental coincidence events

Even though care has been taken to minimize natural radioactivity in the detectors materials, it mainly remains two types of accidental events : $\gamma - \gamma$ and $\alpha - \gamma$ coincidences. In order to reduce the first kind, we use all the detector's properties concerning the neutron capture selection: unicity in a cell at a level of a few photoelectrons, energy and pulse shape discrimination. In the second type of coincidences alpha pulses are quite similar to those of neutron capture but the energy. Special care was taken to decrease the alpha radioactivity associated with the uranium contamination of the lithium compound. In modules 2 and 3, liquids are slightly contamined at a level of 1 ppb. So the accidental background in these modules is higher than in module 1 (Table 6).

Energy spectra and time distributions between positron and neutron candidates are shown in Fig.24 and 19.

Table 6: Accidental background rates in reactor "ON"

module 1	$1.17 \pm 0.03\ evt\ h^{-1}$
module 2	$2.68 \pm 0.04\ evt\ h^{-1}$
module 3	$1.92 \pm 0.02\ evt\ h^{-1}$

9.3 Correlated events

The correlated component of the background is similar in the 3 detectors. It has mainly two origins: The fast neutrons originating from cosmics interactions and the natural radioactive cascade of ^{214}Bi.

Fast neutrons from cosmics interactions: A wide spectrum of neutrons are created by the muonic component of cosmic rays in the surrounding materials of the detector. Direct muon hits are rejected with an inefficiency lower than 1 % with the veto counters, but neutrons are only partially rejected. Fast neutrons can produce recoil proton pulses and slow neutrons in the detector. The slow neutron thermalizes in the scintillator and is captured by ^{6}Li , faking a full anti-neutrino event. Pulse shape properties of the scintillator are used in order to discriminate proton recoil pulses from neutrino positron pulses so then reduce this component of the background. Fig.23 shows PSD spectra of all "prompt" candidates. We can see the contribution of protons recoiling from fast neutrons in the neutron thermalization process. Part of these protons survive the positron PSD cut. Table 7 shows the observed rates of this type of background with the three modules of detection.

Table 7: Background rates in h^{-1} from cosmic ray induced fast neutrons

	ON	OFF
module 1	1.2 ± 0.4	0.7 ± 0.2
module 2	0.6 ± 0.2	0.6 ± 0.2
module 3	0.7 ± 0.2	0.5 ± 0.2

As can be seen in Table 7 and in Fig.23 the magnitude of the peak at high positron PSD is the same for reactor-on and off periods thus this kind of background is eliminated by the subtraction On-Off.

"Bismuth-events": ^{214}Bi is one of the element of the natural radioactive family of ^{238}U which follows ^{222}Rd. However the contamination in ^{222}Rd does not come from equilibrium with uranium impurities found in liquid scintillators. It originates probably from optical tunnels stainless steel. ^{214}Bi is a beta emitter and gives ^{214}Po:

$$^{214}Bi \longrightarrow ^{214} Po + e^{-}(Q = 3.27MeV)$$

$$^{214}Po \longrightarrow ^{210} Pb + \alpha(Q = 7.8MeV, \tau = 236\mu s)$$

The 7.8 MeV alpha kinetic energy is detected as a 820 keV electron energy. The electron simulates the positron interaction and the alpha the neutron capture of the anti-neutrino event with a significantly higher energy. However due to resolution smearing a small fraction of these events induces a correlated component of the background. Fig.22 shows neutron candidate energy spectra when the PSD stays within $\pm 2.2\,\sigma$ around the mean and no energy cut is applied. We recognize the ^{214}Po alpha peak. Integration between $\pm 2.2\,\sigma$ of the mean gives rate of bismuth events which are presented in Table 8. Naturally these events do not all induce background, but they allow us to check independently the quality of our neutrino analysis by verifying that the bismuth events remain constant over the neutrino data taking period.

Table 8: Bismuth-event rates

module 1	$8.91 \pm 0.09\, evt\, h^{-1}$
module 2	$13.87 \pm 0.09\, evt\, h^{-1}$
module 3	$14.33 \pm 0.09\, evt\, h^{-1}$

The part of the bismuth-events that induces background has been estimated by the data taken in reactor-on and off periods separately. We made use of the fact that the ^{214}Po lifetime (236 μs) is much longer than the neutron capture time (30 μ s). Table 9 shows the average rate of that part of the "Bismuth-events" in the three detection modules which satisfies the data selection criteria and thus contaminates the neutrino events. As can be seen (cf. also Fig.22) the background event rates are the same in the reactor-on and off periods, therefore a simple subtraction On-Off can eliminate this background.

Table 9: Average "Bismuth-event" background rates

	ON	OFF
module 1	0.52 ± 0.03	0.52 ± 0.06
module 2	0.19 ± 0.07	0.24 ± 0.04
module 3	0.12 ± 0.05	0.05 ± 0.03

Reactor off rates: When all cuts are applied the residual correlated background measured during the reactor off period is of 2.22 ± 0.06 *evts* h^{-1} in detector 1 and 1.32 ± 0.06 *evts* h^{-1} in detector 2 and 1.15 ± 0.05 *evts* h^{-1} in detector 3. Energy spectra and time distributions between positron and neutrons candidates of the residual correlated background are shown in Fig.24 and 19.

9.4 Neutrino signal

The observed event rates are corrected for the dead-times of the detector modules and for losses due to electronics or HV power failures in some detection channels. The neutrino signal is then obtained by subtracting first the accidental background from the data separately in the reactor-on and off periods. Next, the remaining events from the reactor-off period are subtracted from that of reactor-on period. The signal event rates are finally corrected for the expected number of neutrino events from far away reactors. They are summarized in Table 10 with the signal-to-background ratio for 15, 40 and 95 meters, respectively.

Table 10: Average signal event and total background rates in h^{-1} at the three distances

	15 m	40 m^*	95 m
Signal event rate	62.62 ± 0.23	15.39 ± 0.17	1.38 ± 0.20
Total background rate (without ν's from far reactors)	2.50 ± 0.07	6.94 ± 0.09	1.96 ± 0.18
Signal/Background	25.0	2.2	0.7

* For the two modules

The positron spectrum normalized to a nominal 2800 MW thermal power is presented in Fig.24 for the 15 meter station, together with the two backgrounds spectra.

9.5 The Bugey 3 detector as a fast neutron calorimeter

Besides the neutrino detection, our detector (or any adapted replica of an elementary cell) can be operated as a very selective fast neutron detector. A neutron with a kinetic energy above 1 MeV is unambiguously identified by a recoil proton signal followed within 30 μs by a signal of an alpha-triton pair produced in the thermal neutron capture reaction. The PSD method allows a very clean identification of the charged particles with a discrimination factor better than 10^3 against the Compton electron background. The measure

of the proton recoil energy deposition allows to obtain the detected neutron energy, in possible association with a time-of-flight measurement.

Such an utilization has been performed in underground laboratories (Laboratoire Souterrain de Modane, Gran Sasso [36]) in order to measure the fast neutron residual natural background. At the Modane site a limit of 1.1 ± 0.1 neutron event per day has been measured in an elementary cell. The experiment is presently continuing taking data in order to understand the origin of these neutrons. Another side application in this field has been a series of measurements of an hypothetic neutron production from "Cold Fusion" electro-chemical experiments. The Bugey set-up of the underground position has been used, as well as a single prototype cell at the Modane site. Negative results were found with very good limits[37].

10 Conclusion

We have described here the use of a novel neutrino detector in an neutrino oscillation search. The detector is characterized by its high efficiency, compacity, its good time and spatial confinement of the neutrino event, its high selectivity leading to a signal to noise ratio ratio of 25 obtained at 15 meter from a 2800MW reactor. The calorimetric functions of the detector have been monitored and controlled within an accuracy lower than a percent. Such a neutrino detector is also manifestly an excellent large solid angle fast-neutron calorimeter giving a very constrained neutron signature and a powerful gamma rejection.

11 Acknowledgements

We wish to dedicate this work to the memory of R.Provasi, J-F.Thomas and J-P Wuthrick.

This work has been supported by the Institute of Nuclear and Particle Physics (IN2P3-CNRS), the Commissariat à l'Energie Atomique (CEA-DSM-DAPNIA) and the French Electricity Company (EDF).

We are specially grateful to the EDF staff, whose help has been essential for the sucessful running of this set-up at Bugey.

References

[1] F.Reines and C.L.Cowan, Physical Review 92 (1953) 830

[2] J-F.Cavaignac *et al.*, Physics.Letters 148B (1984) 387

[3] M.Talby, Proc. XXVIth Int. Conf. on High Energy Physics, Munich 1989, ed. by R.Kotthaus, J.Kühn (Springer Verlag, Berlin-Heidelberg, 1989) 1072
M.Talby, Recherche des oscillations neutrinos auprès d'un réacteur. Thèse pour obtenir le titre de Docteur d'Etat-Sciences, Marseille, 1988.
M.Talby, Proc. XXIIth Rencontre de Moriond, The Standard Model, the Supernova 1987A, page 393. Edited by J.Tran Tan Vanh, edition Frontières, 1987.
H. de Kerret, Proc. XXIIIth Rencontre de Moriond, The 5th Force, Neutrino Physics, page 125. Edited by J.Tran Tan Vanh, edition Frontières, 1988.

[4] B.Achkar *et al.*, Nuclear Physics B534 (1995) 503

[5] see for instance: E.Pasierb *et al.*, Phys.Rev.Letters 43 (1979) 96
G.S Vidyakin *et al.*, J.Moscow Phys.Soc. 1 (1991) 85
A.Etenko *et al.*, Physics Letters B338 (1994) 383.

[6] see for instance: H.Kwon *et al.*, Phys.Rev. D24 (1981) 1097
G.Zacek *et al.*, Phys.Rev. D34 (1986) 2621
J-F.Cavaignac *et al.*, Physics.Letters 148B (1984) 387

[7] see for instance:
A.I.Afonin *et al.*, Sov.J.Nucl.Phys. 46 (1987) 944
H.de Kerret *et al.*, "The Chooz experiment proposal"

[8] NE320, produced by Nuclear Enterprise, Edinburg, U.K.
NE172,NE235H: other products used in this experiment

[9] S.Ait-Boubker *et al.*, Nuclear Instr. and Methods A277 (1989) 461.

[10] A.Stutz, Conception par simulation et réalisation d'un détecteur d'antineutrinos. Thèse pour obtenir le titre de Docteur de l'Université Joseph Fourier - Grenoble I, ISN Grenoble, 1989.

[11] The tank has been manufactured in SDMS company, St-Marcellin 38 France

[12] Teflon FEP type 500A for tunnels, 500C for windows (DuPont de Nemours International S.A)

[13] EPO-TEK 301-2 (EPOTECNY)

[14] Q2-3067 (DOW-CORNING)

[15] GORE-TEX, W.L.Gore and Associates (Inc)

[16] G.Cocconi and V.Cocconi, Phys.Rev. 84 (1951) 29

[17] S.Ait-Boukner,Etude sur prototype et par simulation d'un détecteur d'antineutrinos à base de scintillateur chargé au lithium-6. Thèse pour obtenir le titre de Docteur de l'Université Joseph Fourier - Grenoble I, ISN 92.100, Grenoble, 1989.

[18] B.Achkar, Recherche d'oscillations de neutrinos auprès d'un réacteur nucléaire. Thèse pour obtenir le titre de Docteur de l'Université Joseph Fourier - Grenoble I, ISN 92.100, Grenoble, 1992.

[19] C.L. Morris, Nuclear Instr. and Methods 137 (1976) 397

[20] Photomultipliers DATA HANDBOOK Book PC04 PHILIPS (1990)

[21] J.Pouxe, Rapport Interne ISN 88-43
Discriminateur d'amplitude à fraction constante 8 voies

[22] B. Guerre-Chaley et J.Pouxe, Rapport Interne ISN 89-32
Unité de traitement analogique UTA

[23] R. Aleksan *et al.*, Nuclear Instr. and Meth. A273 (1988) 303

[24] J.Berger *et al.*, Nuclear Instr. and Methods A279 (1989) 343

[25] P.Besson, doctorat thesis, LAPP(Annecy), 1989.

[26] ORIEL, Box 872, Staford, CT, USA

[27] J-P.Cussonneau, Comparaison entre la simulation et les données de neutrinos dans BUGEY 3. Thèse pour obtenir le titre de Docteur en Sciences Physiques, LPC 92T1, Paris, 1992.

[28] see for instance: R.Diehl and U.Grasser, Nuclear Instr. and Methods A186 (1981) 665. D.T.Ingersoll and B.W.Wehring, Nuclear Instr. and Methods A147 (1977) 551.

[29] H. de Kerret, B.Lefièvre, Simulation des neutrons de basse énergie par Monte Carlo, Collège de France, LPC 88-01.

[30] Drozdov *et al.*, Proceedings of the IInd Int. Conf. on The Peaceful Uses of Atomic Energy Vol 16, (1958)

[31] V. McLane, Ch. L. Dunford and Ph. F. Rose, Neutron Cross Sections, Academic Press Inc. 1988

[32] R.Brun *et al.*, GEANT simulation package, Long Writeup, CERN Program Library W5013.

[33] Y.Dufour, Comparaison entre la simulation et les premières données de Bugey III. Thèse pour obtenir le titre de Docteur ès Sciences Physiques, LPC T 89 01, Paris, 1989.

[34] H.H.Seliger, Phys.Rev. 88 (1952) 408

[35] H.H.Seliger, Phys.Rev. 100 (1955) 1029

[36] R.Aleksan *et al.*, Nuclear Instr.and Methods A274 (1989) 203

[37] F.Botter *et al.*, Phys.Letters B232 (1989) 536
R.Aleksan *et al.*, Phys.Letters B234 (1990) 389
D.Aberdam *et al.*, Phys.Rev.Letters 65 (1990) 1196

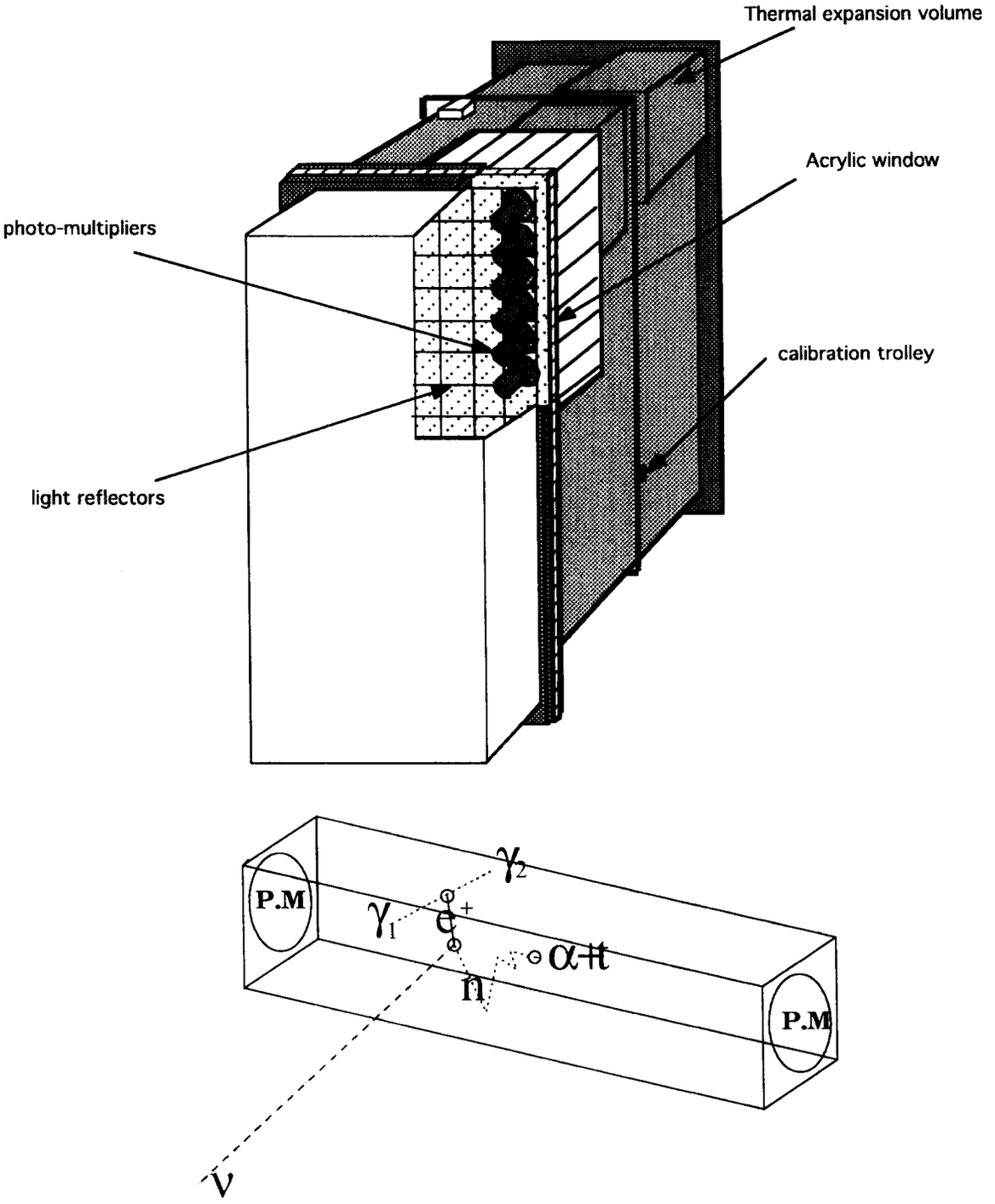

Figure 1: A schematic view of one detection module and of the detection principle

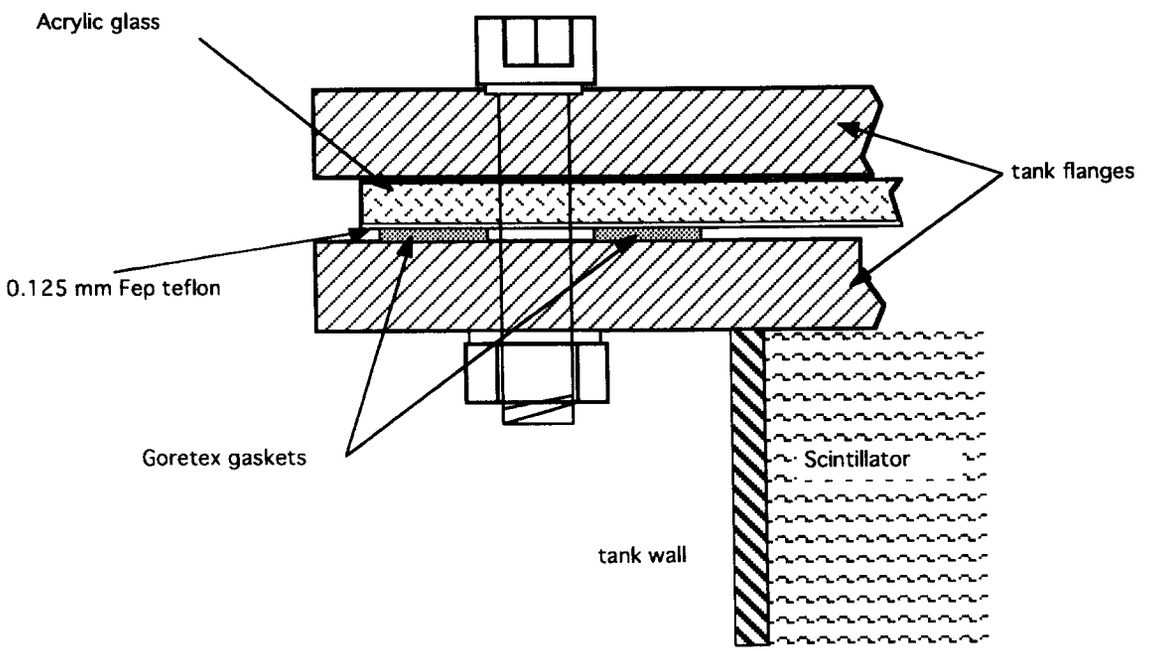

Figure 2: A detailed view of the gasket region

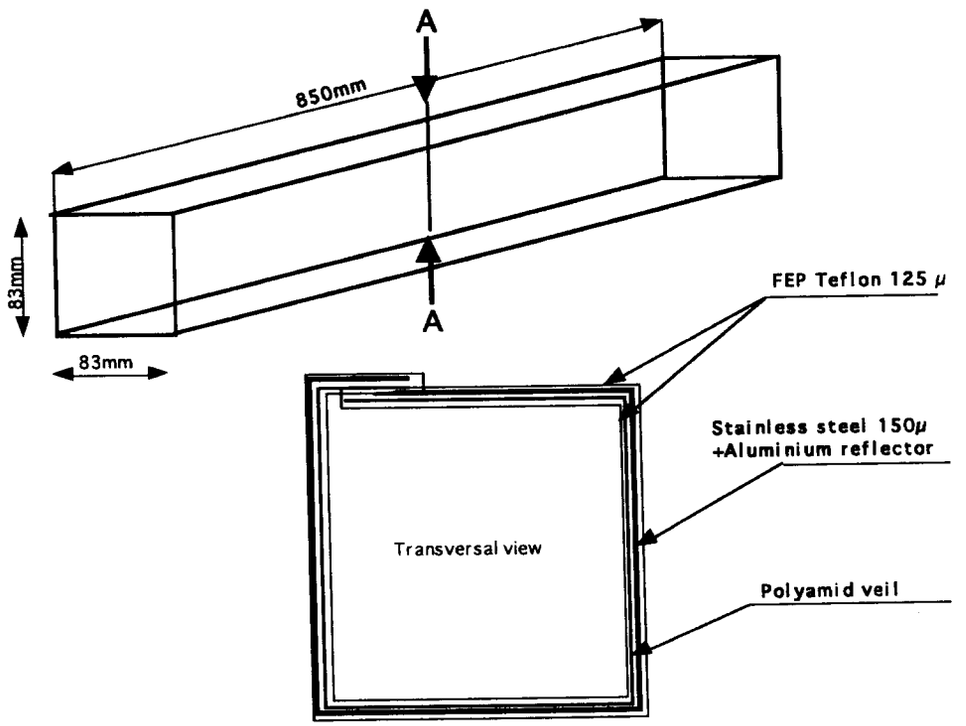

Figure 3: Main features of one internal light collector

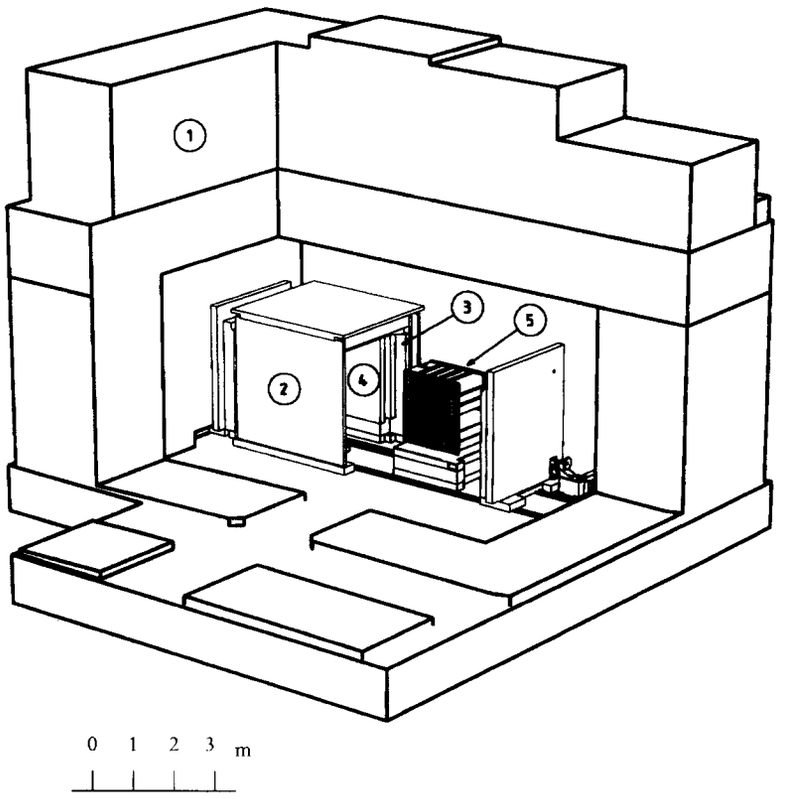

1 Concrete blocks

2 Iron wall (15 cm thick)

3 Tank of 25 cm of water+0.5 cm B4C

4 Veto wall+0.1 cm mumetal

5 The two detectors of position 2

Figure 4: The shielding bunker at the 40 meter station

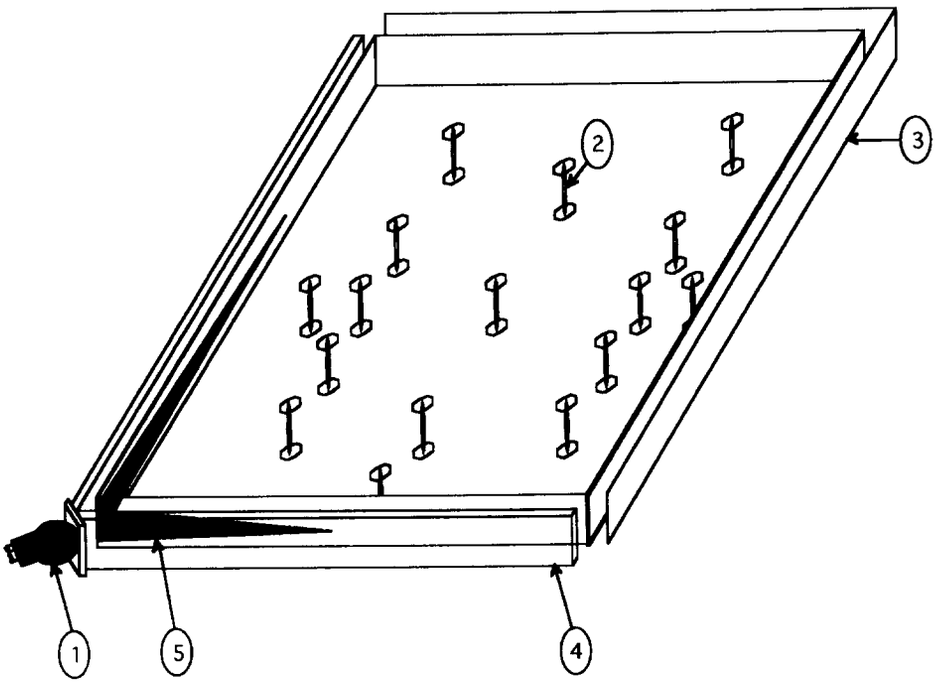

Figure 5: The anti-cosmic detectors: (1) photo-multiplier, (2) metal struts, (3) diffusing reflectors, (4) wavelength shifter, (5) light collection equalizing mask

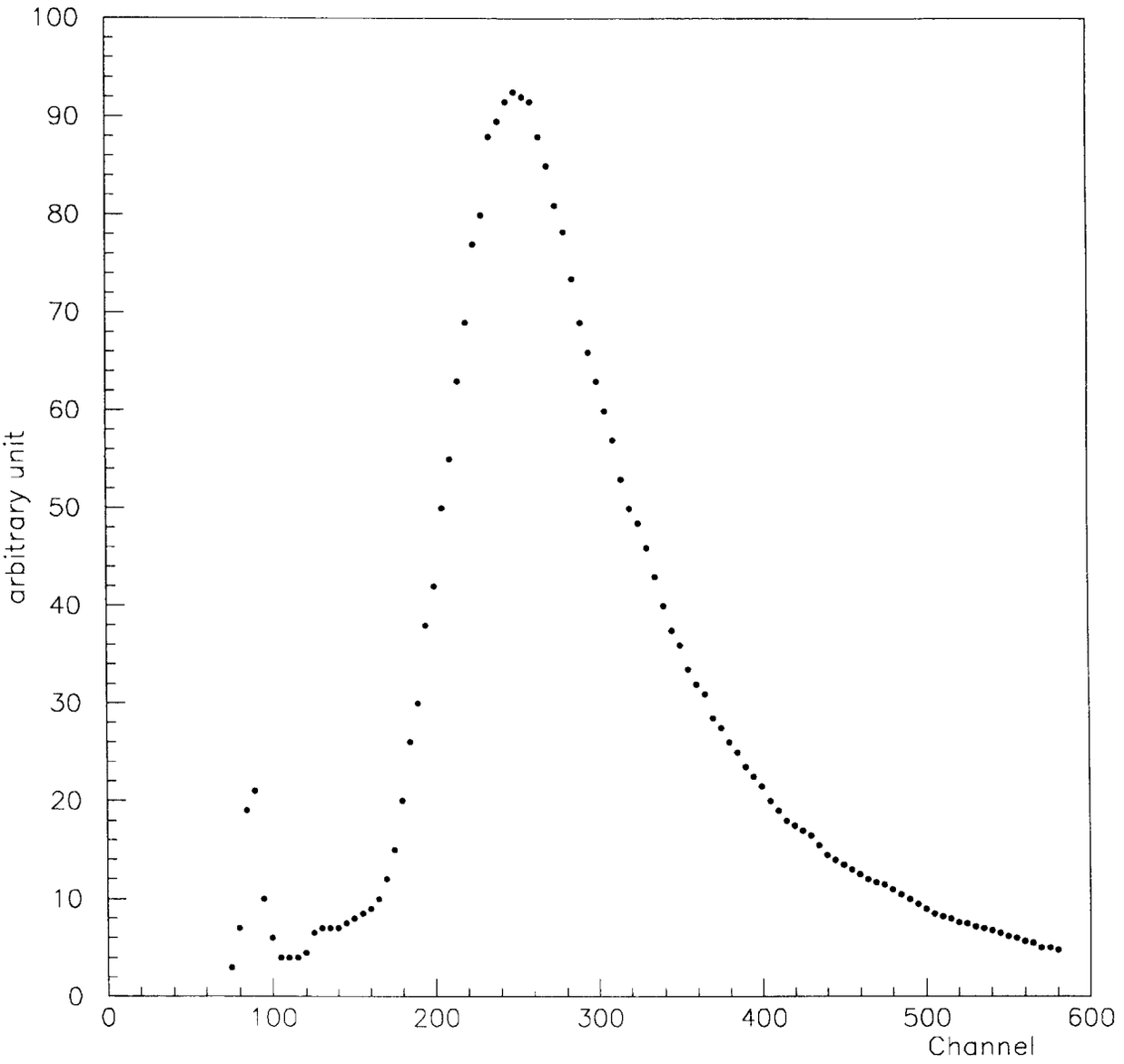

Figure 6: Energy deposited by cosmic muons in the 2.5 m^2 roof veto

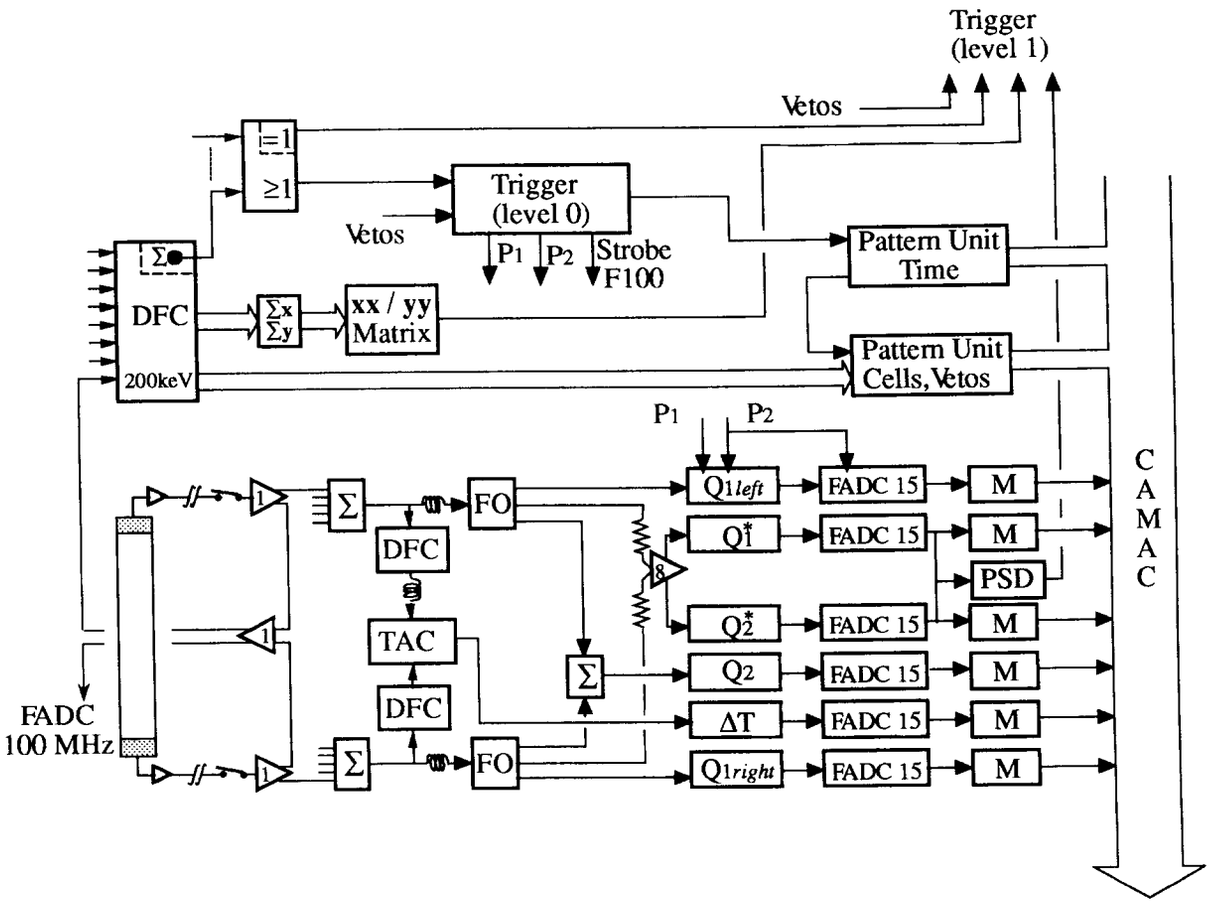

Figure 7: Electronics set-up

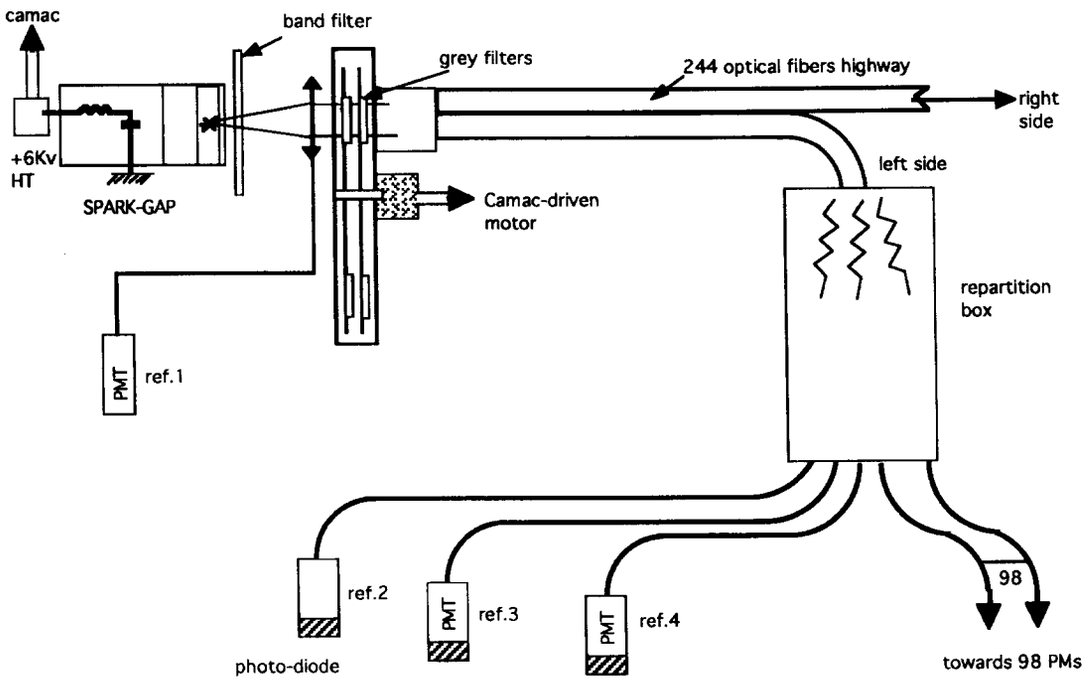

Figure 8: The artificial light-test network

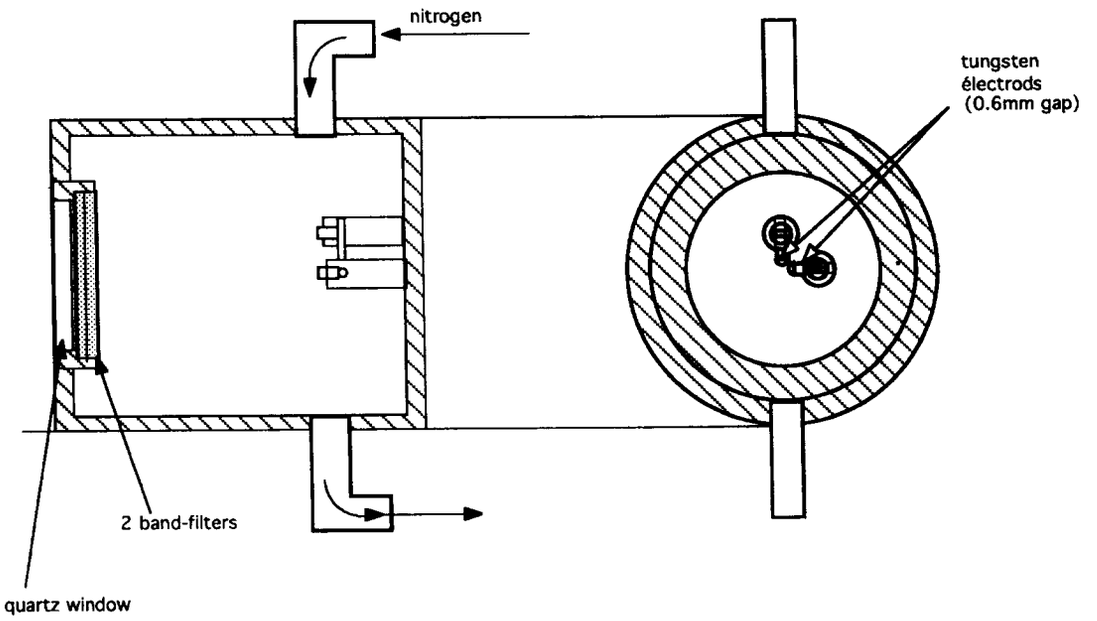

Figure 9: Details of the light pulse generator

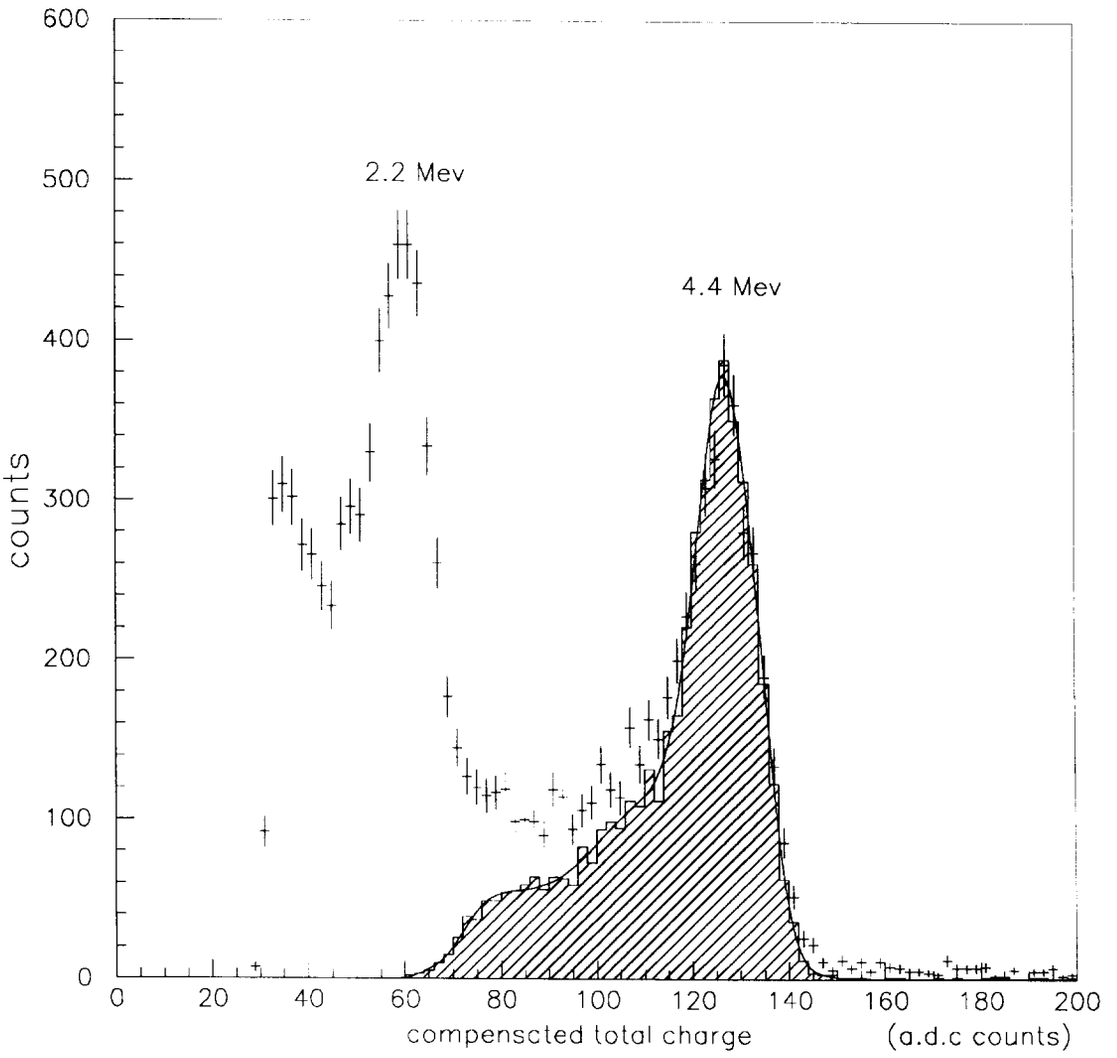

Figure 10: The Compton edge of the $4.4 MeV$ photon obtained with an *Am-Be* source. The solid line is the smoothing of the the Monte Carlo simulation histogram (including the threshold effect of the calibration run). The peak near 2 MeV corresponds to gammas from the capture of neutrons in hydrogen not included in this simulation.

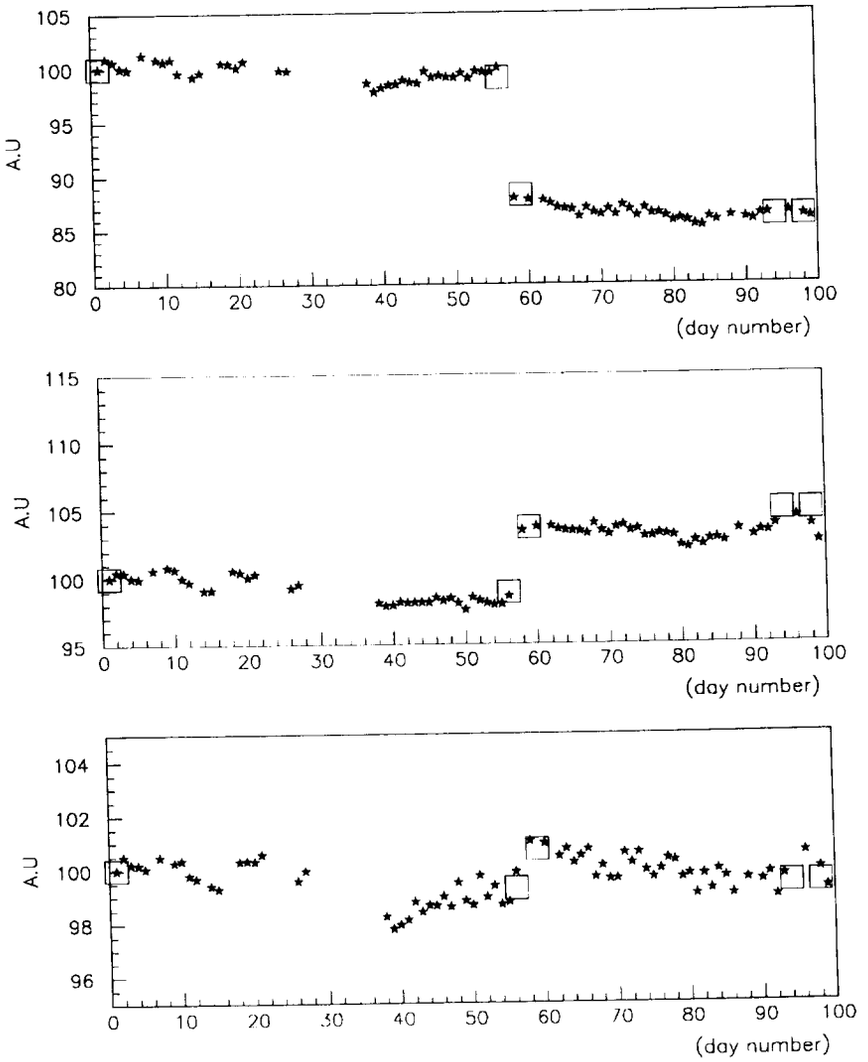

Figure 11: Typical day-to-day gain variations of three channels measured with the help of a monitored nitrogen spark-gap light-pulser. The jumps correspond to readjustments of the high voltage setting point. The results of the calibration with the *Am-Be* source are shown by the squares.

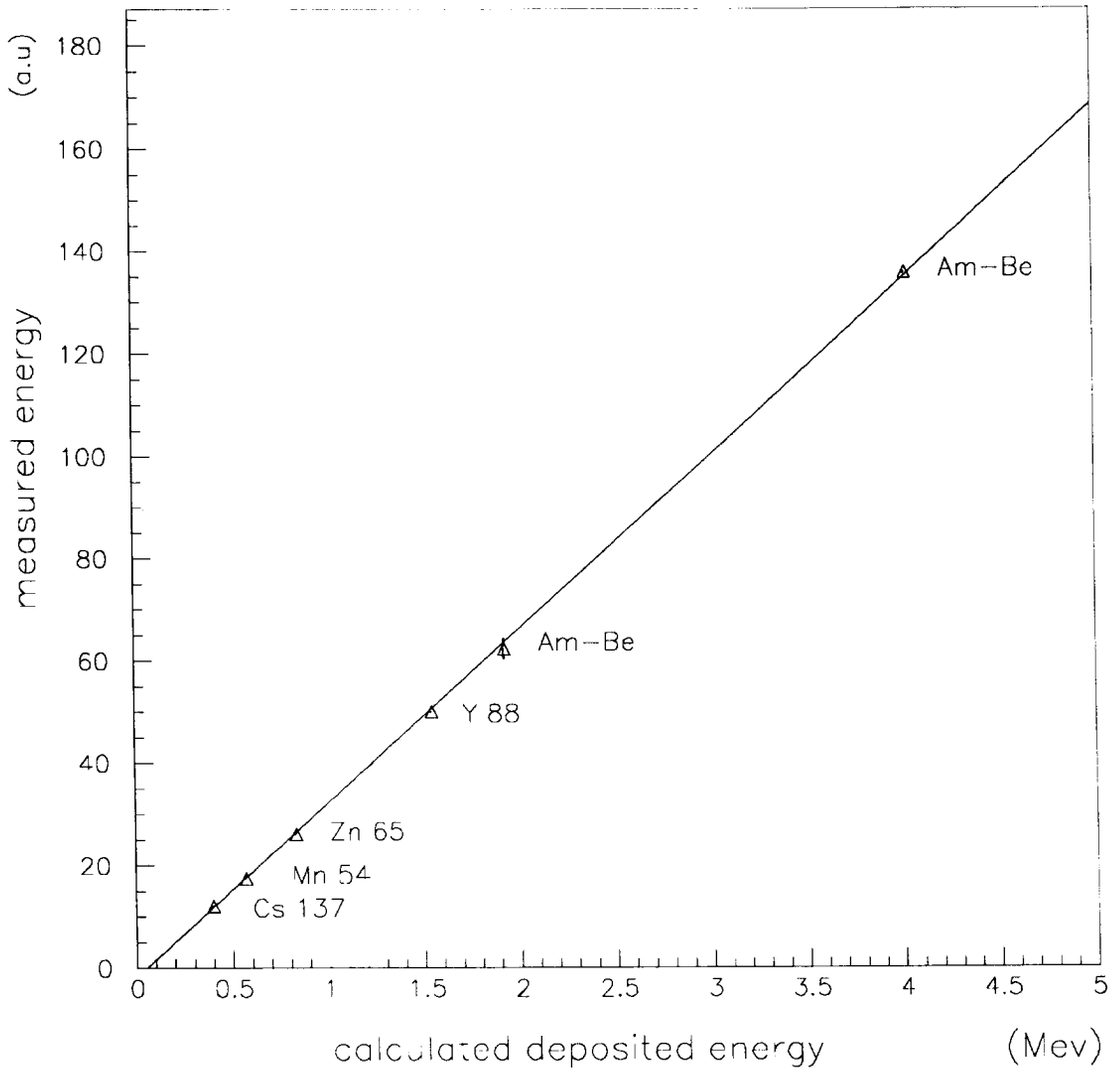

Figure 12: The total charge measured at the end of the opto-electronic chain as a function of the deposited energy calculated by Monte Carlo for different gamma sources. The error bars are smaller than the symbols except at the 2 MeV peak which corresponds to the neutron capture in hydrogen. The linearity of the detector is clearly demonstrated.

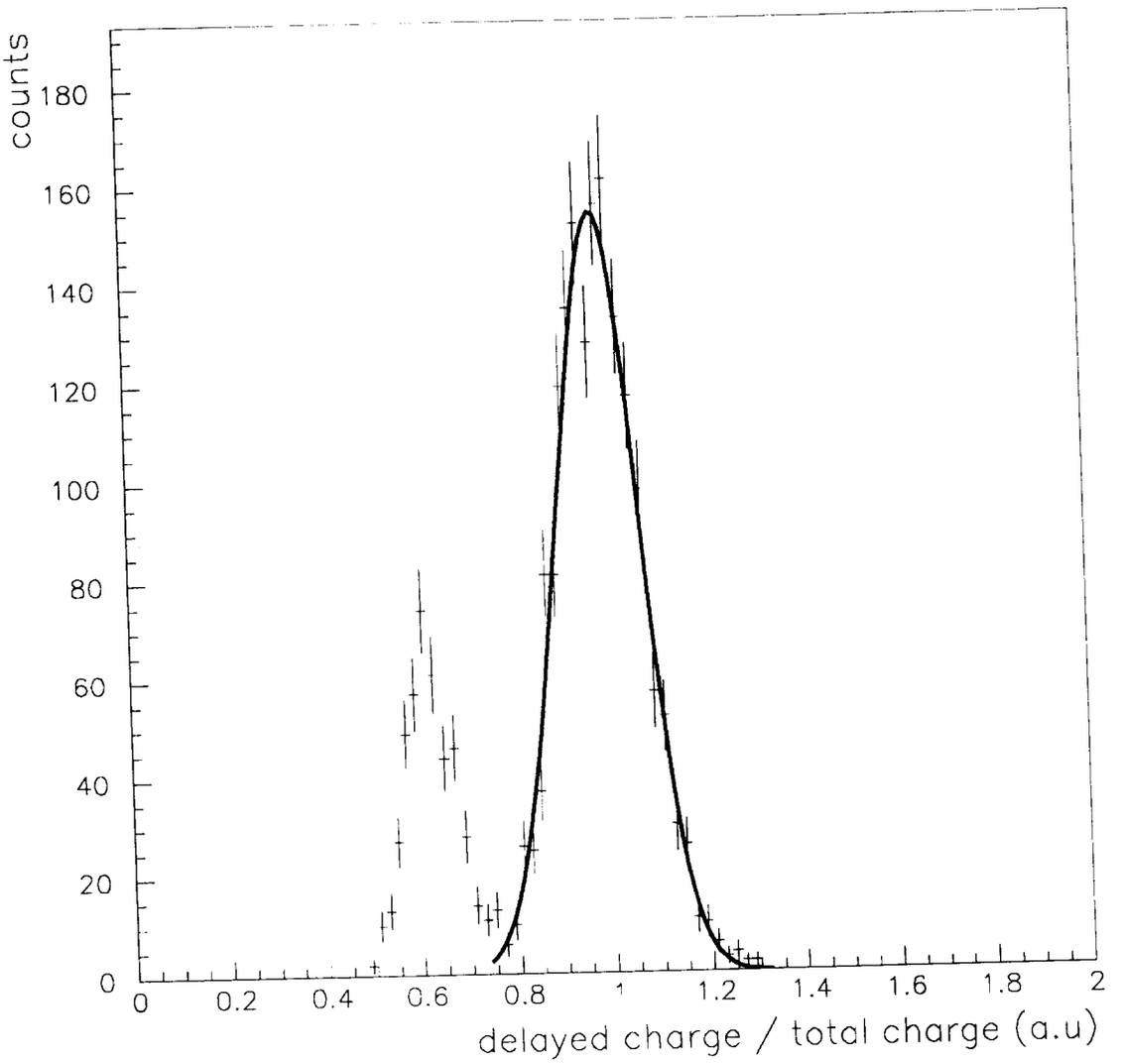

Figure 13: PSD spectrum of neutron capture candidates

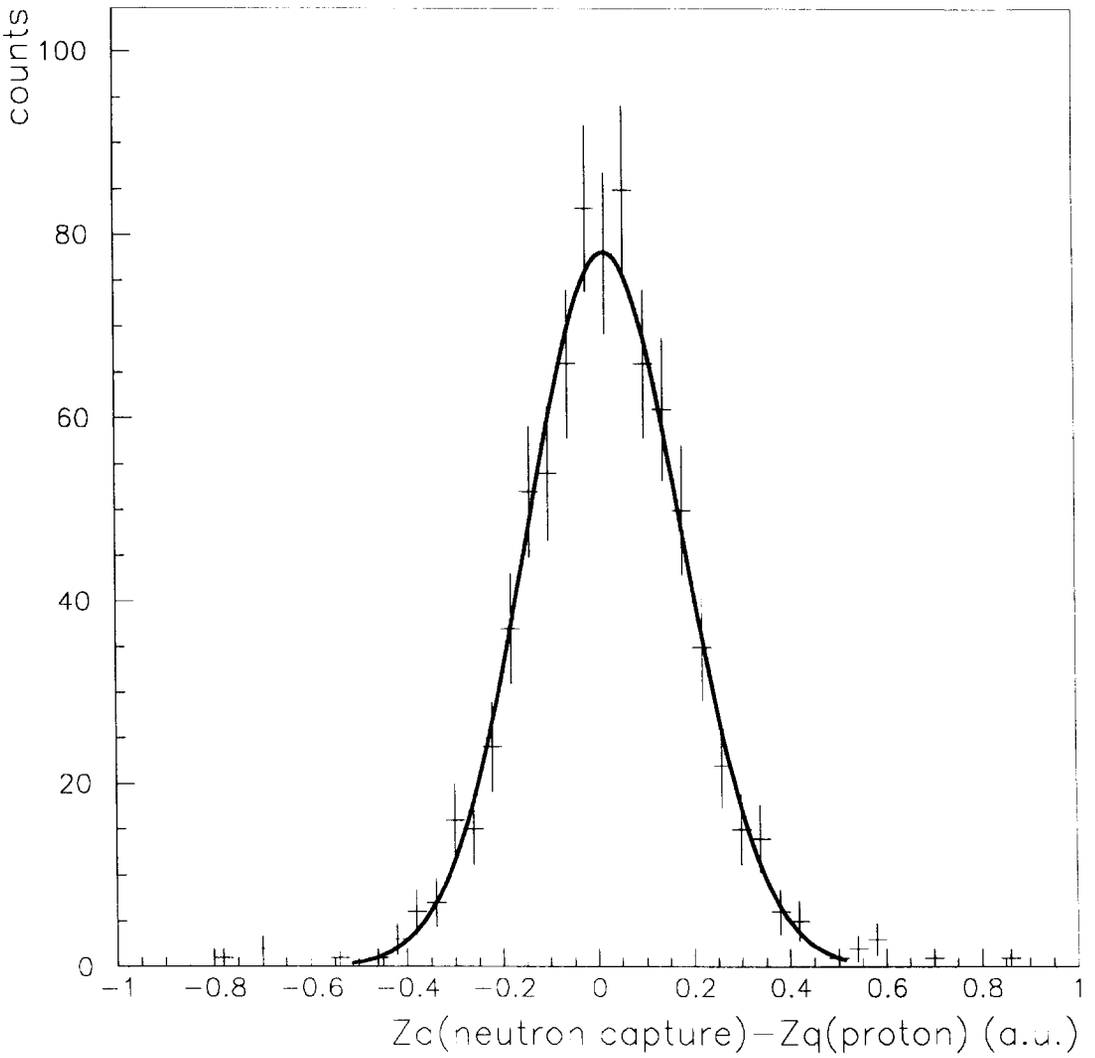

Figure 14: Longitudinal position difference of recoil protons and neutron captures as measured with Z_q

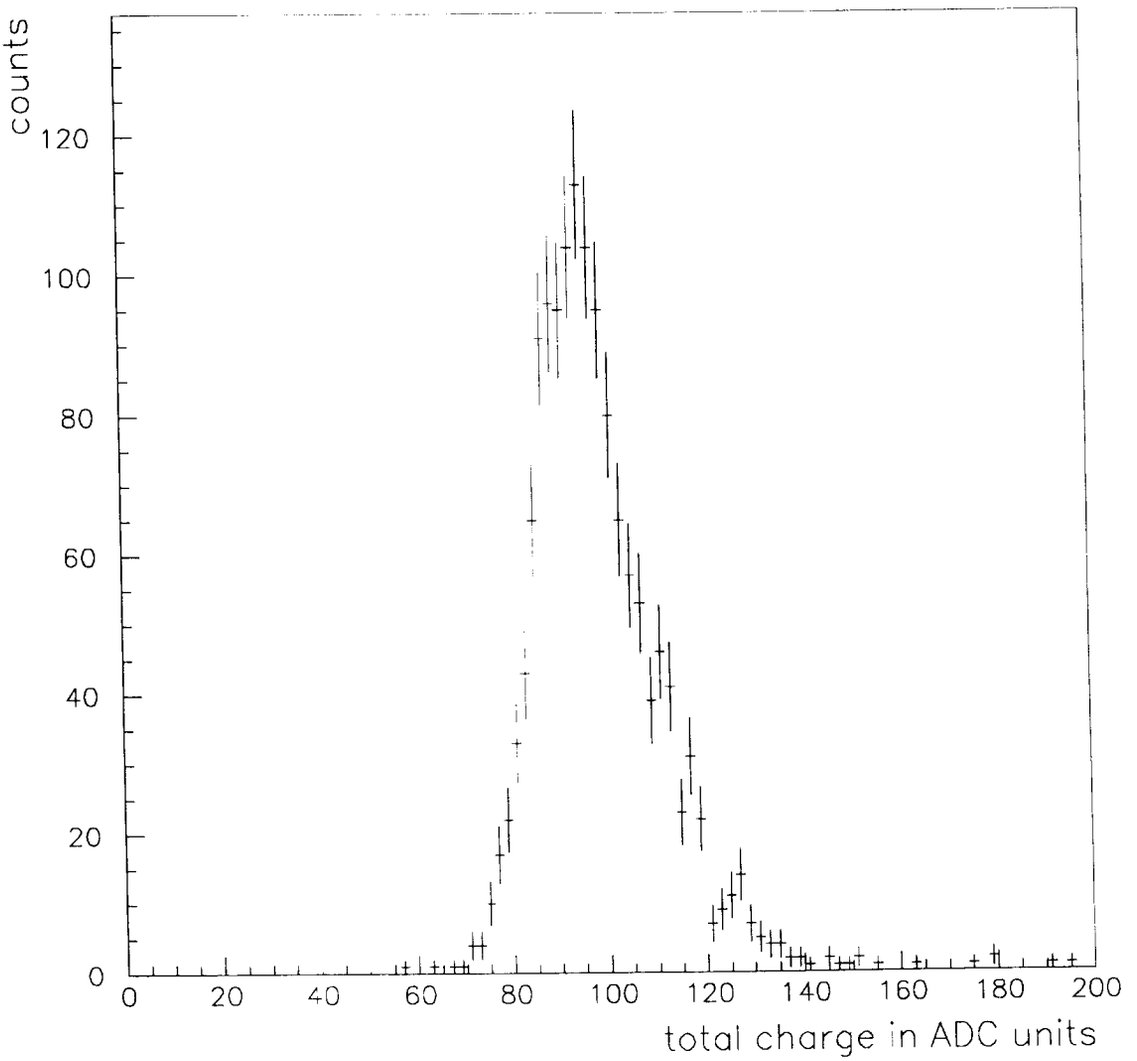

Figure 15: Total charge of final neutron capture events for a typical cell, before Zq correction

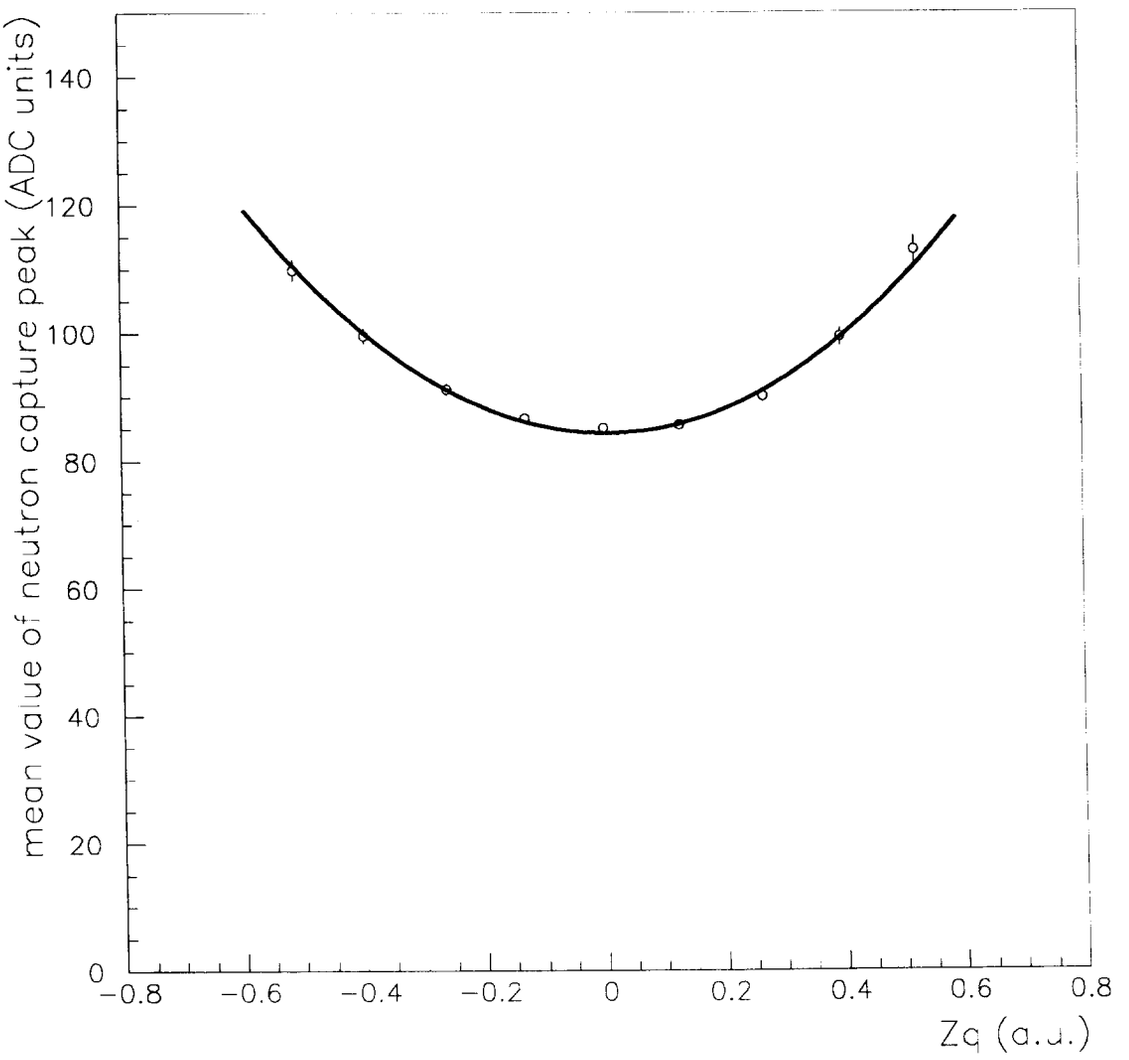

Figure 16: Longitudinal variation of the average total charge produced by neutron captures

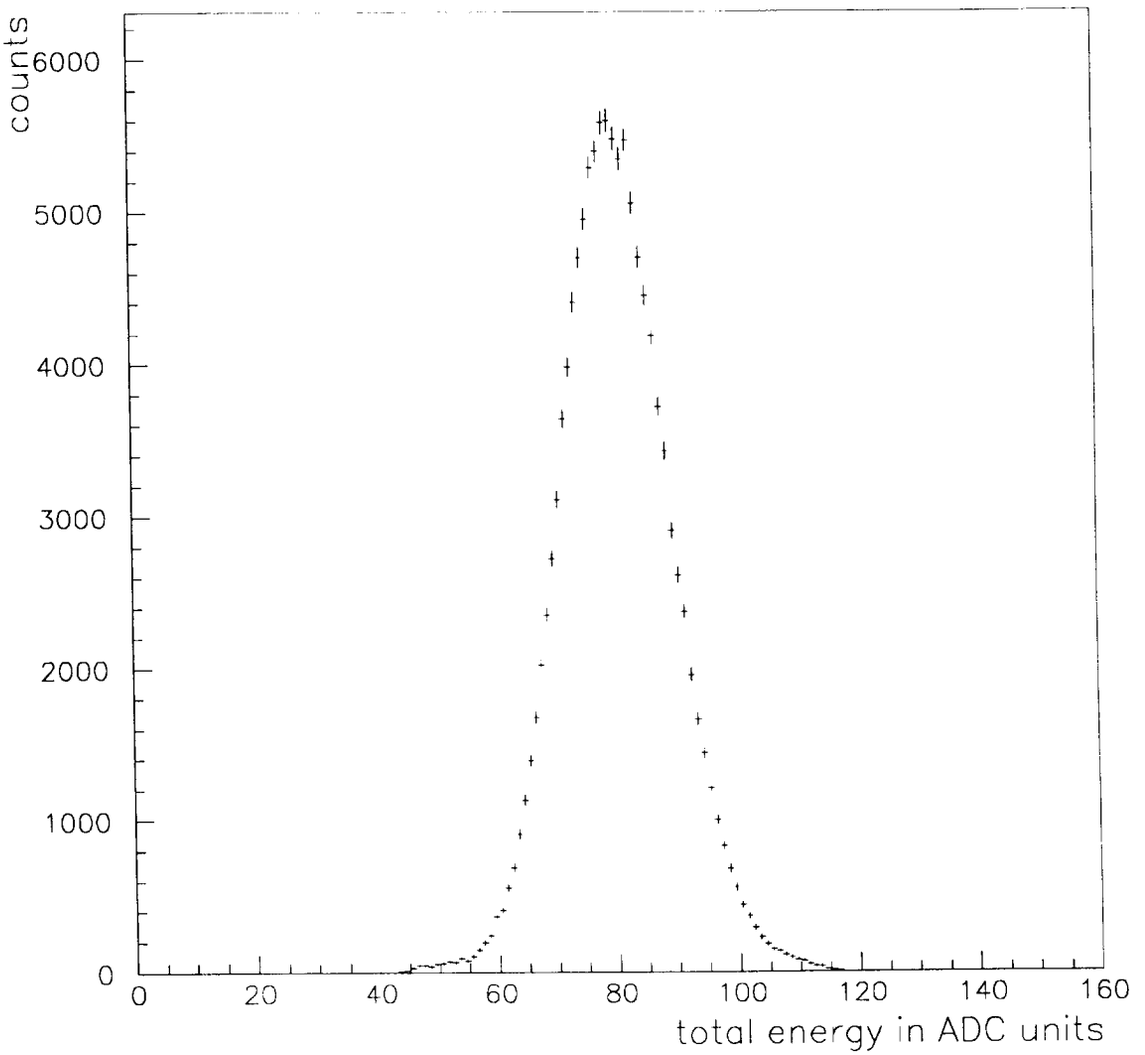

Figure 17: Total charge neutron capture peak as observed over a complete detection module after cell-by-cell alignment

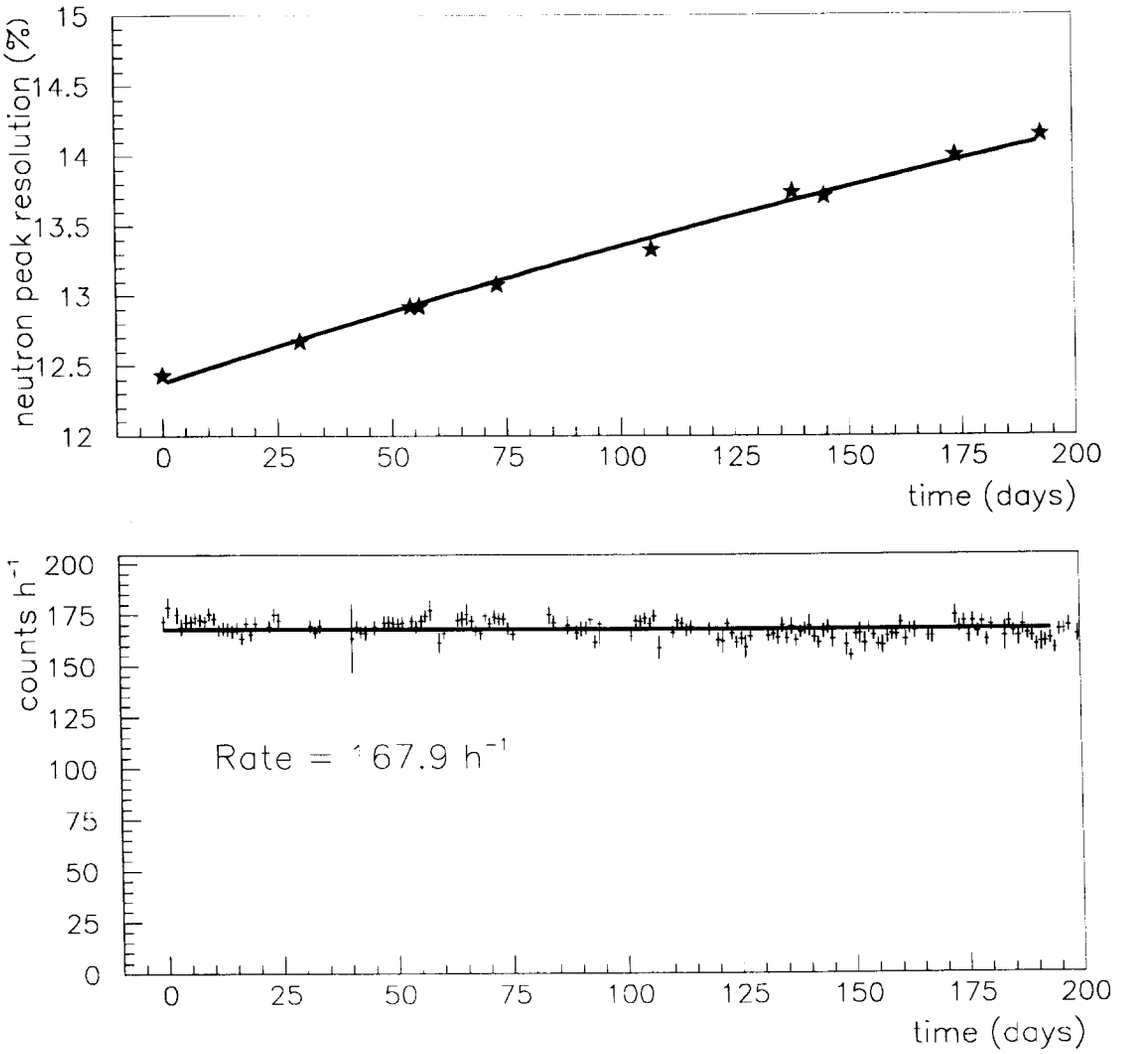

Figure 18: Evolution of the neutron capture peak resolution as a function of time (for module 1) (upper part) and rate of cosmic neutrons recorded during neutrino data acquisition periods for the corresponding days of data taking (lower part)

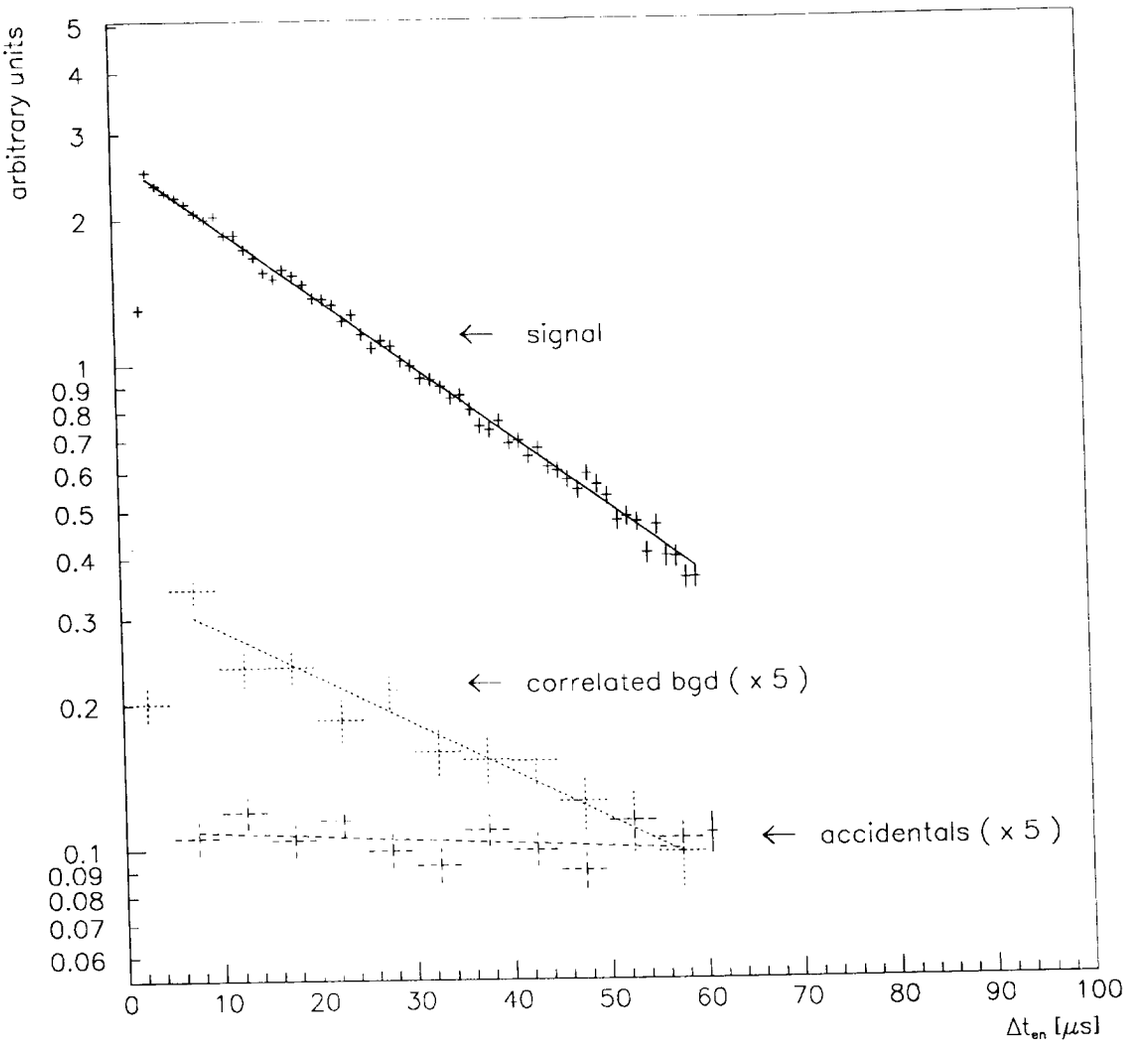

Figure 19: The observed time difference distribution between the positron and the neutron capture signal in module 1 (upper part). Also shown is the slope obtained by Monte Carlo (solid line in the upper part). In the lower part the same experimental distributions with an exponential fit are shown for the accidental and correlated backgrounds.

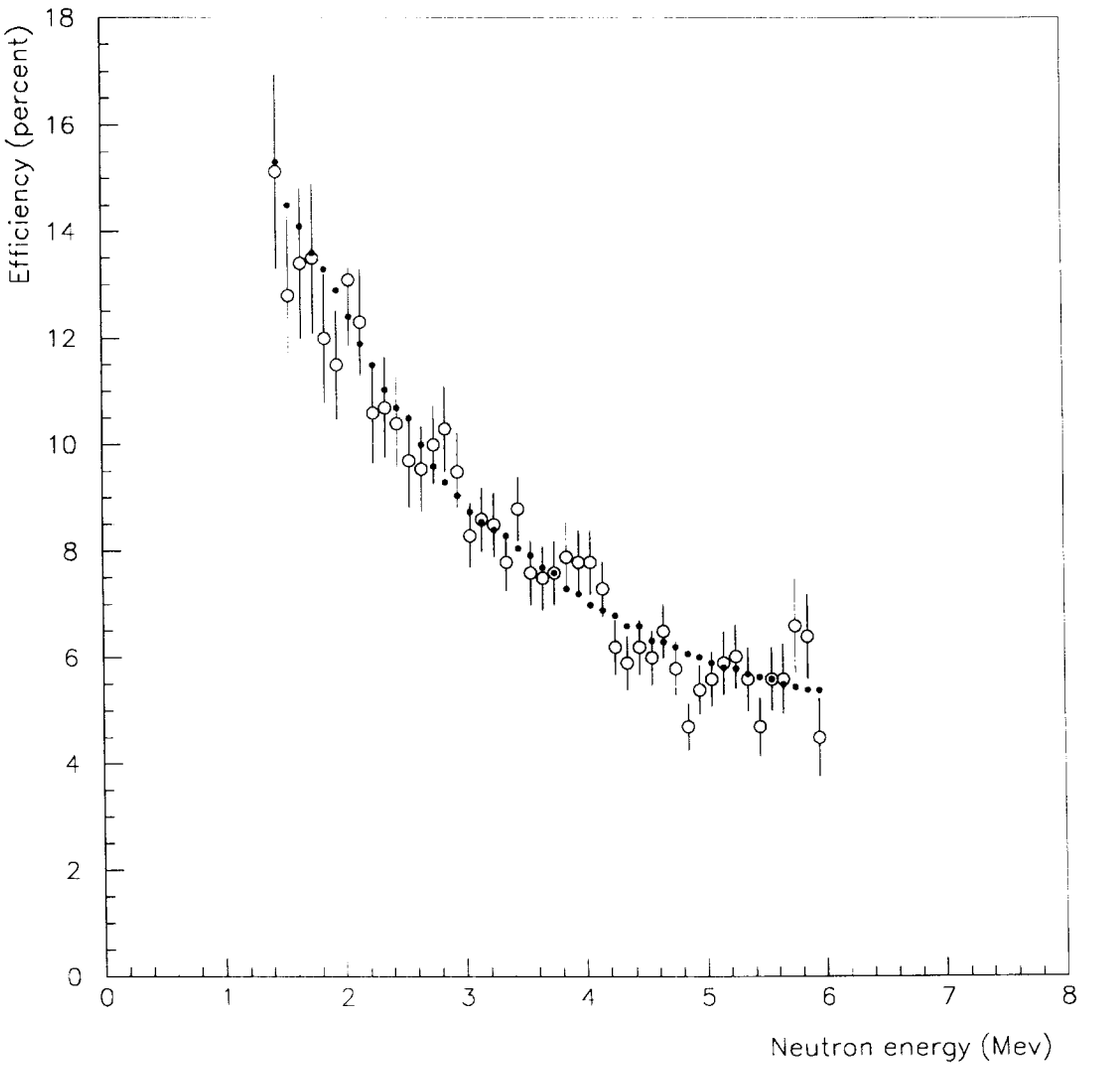

Figure 20: Neutron capture efficiency for fast neutrons having deposited 100 keV equivalent-e^- in the prototype cell as a function of the incident neutron energy; the dots are the neutron Monte-Carlo points.

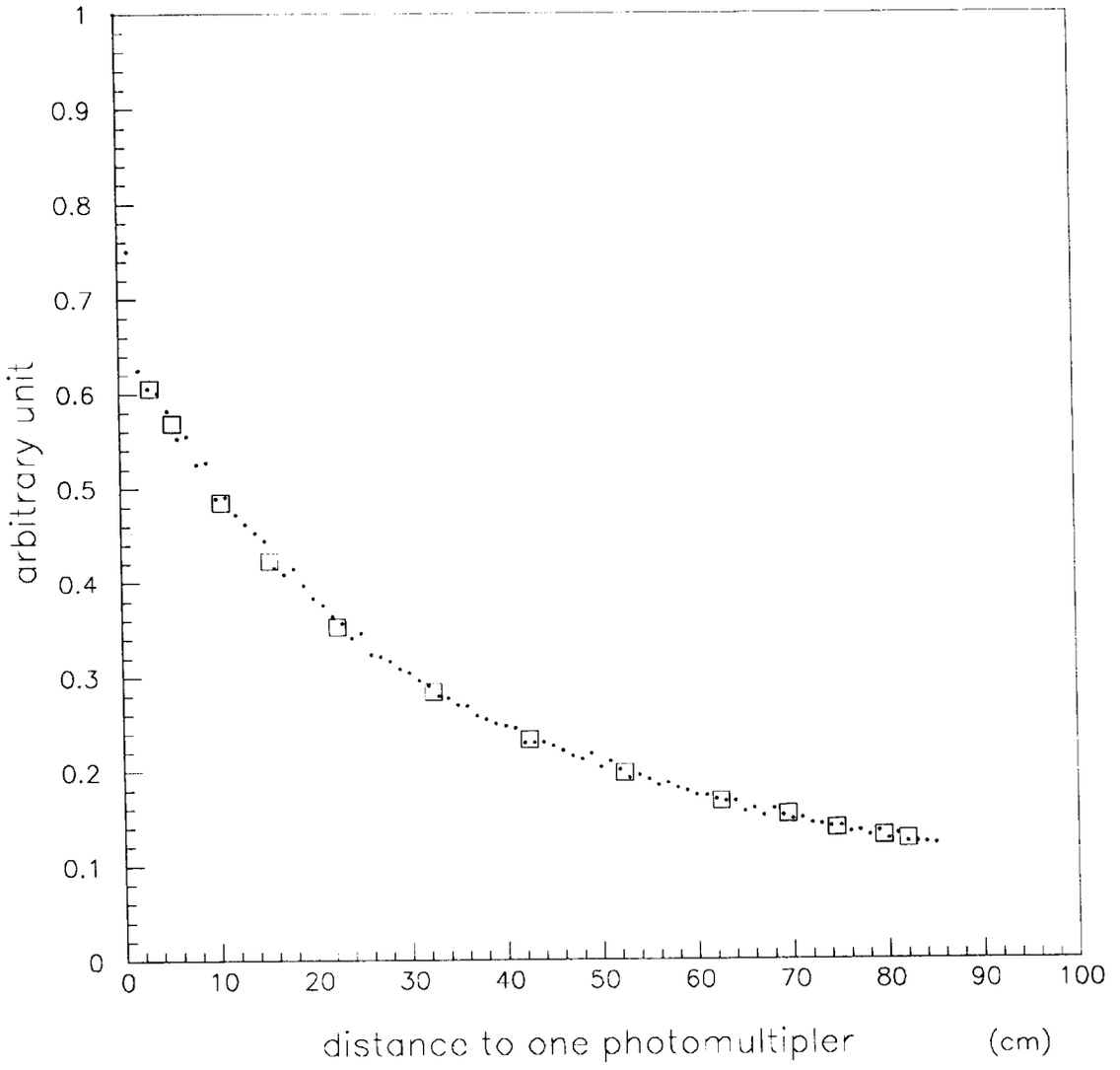

Figure 21: The light collected by one of the two PMT's as a function of the z position of a collimated gamma source used in a Compton backward selection set-up. Squares: data, dotted line: Monte Carlo

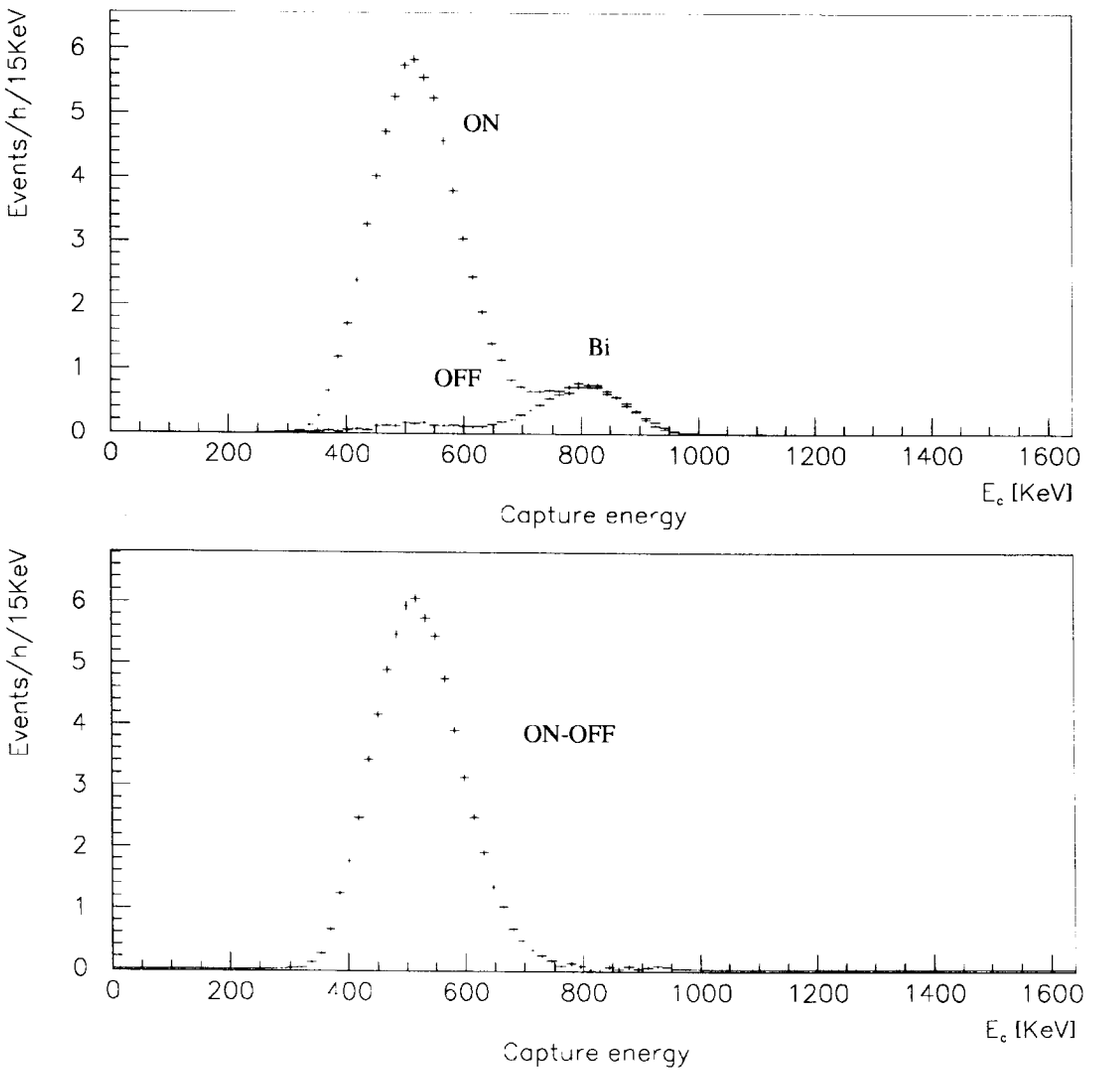

Figure 22: The (e^--equivalent) neutron capture energy spectrum (in *events/h/15 keV*) of the events passing all selection criteria except the neutron energy cut in module 1 for reactor-on and reactor-off periods (upper part) and the difference of the reactor-on and reactor-off periods (lower part).

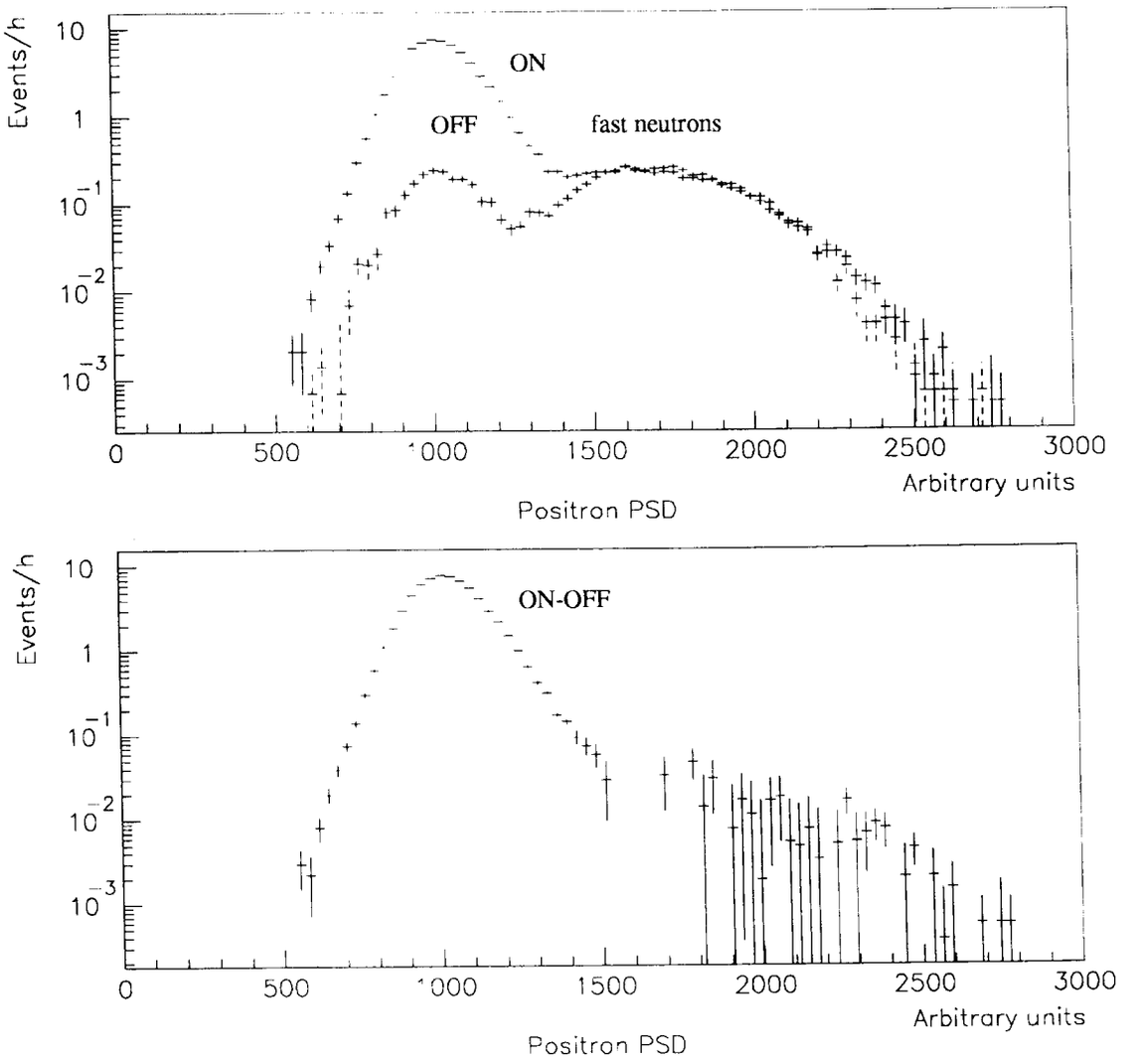

Figure 23: The positron R_{PSD} distribution of the events passing all selection criteria except the positron R_{PSD}-cut in module 1 for reactor-on and reactor-off periods (upper part) and the difference of the reactor-on and reactor-off periods (lower part).

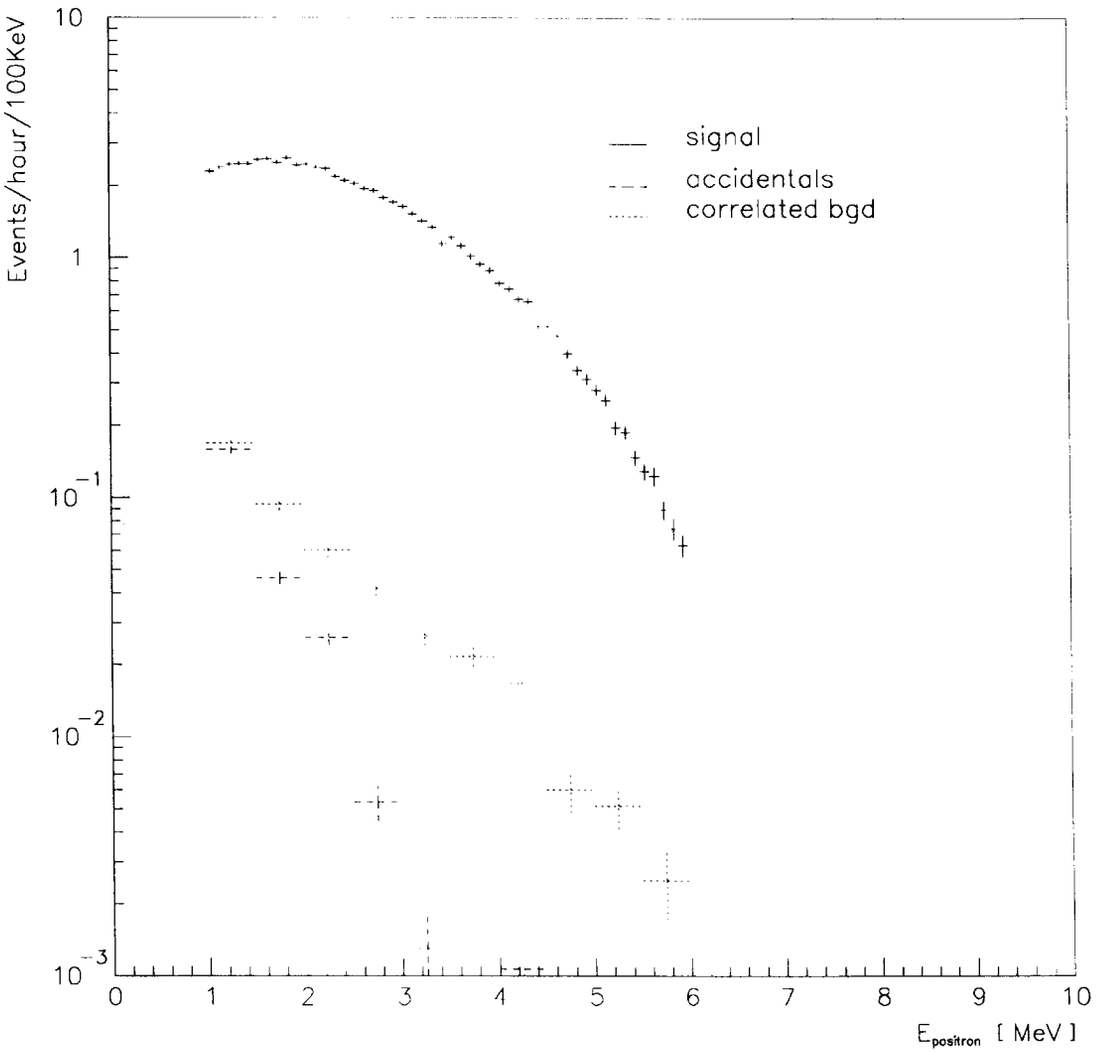

Figure 24: Normalized positron spectra obtained at $15m$ the background being subtracted. The various background components at 15 meter are also shown in the figure.